

Predicting light curves of RR Lyrae variables using artificial neural network based interpolation of a grid of pulsation models

Nitesh Kumar,^{1*} Anupam Bhardwaj,² Harinder P. Singh,¹ Susmita Das,³ Marcella Marconi,² Shashi M. Kanbur,⁴ and Philippe Prugniel⁵

¹Department of Physics and Astrophysics, University of Delhi, Delhi 110007, India

²INAF-Osservatorio Astronomico di Capodimonte, Salita Moiariello 16, 80131, Naples, Italy

³Konkoly Observatory, Research Centre for Astronomy and Earth Sciences, Eötvös Loránd Research Network (ELKH), Konkoly-Thege Miklós út 15-17, H-1121, Budapest, Hungary

⁴Department of Physics and Earth Science, State University of New York at Oswego, Oswego, NY 13126, USA

⁵Université de Lyon, Université Lyon 1, 69622 Villeurbanne; CRAL, Observatoire de Lyon, CNRS UMR 5574, 69561 Saint-Genis Laval, France

Accepted XXX. Received YYY; in original form ZZZ

ABSTRACT

We present a new technique to generate the light curves of RRab stars in different photometric bands (I and V bands) using Artificial Neural Networks (ANN). A pre-computed grid of models was used to train the ANN, and the architecture was tuned using the I band light curves. The best-performing network was adopted to make the final interpolators in the I and V bands. The trained interpolators were used to predict the light curve of RRab stars in the Magellanic Clouds, and the distances to the LMC and SMC were determined based on the reddening independent Wesenheit index. The estimated distances are in good agreement with the literature. The comparison of the predicted and observed amplitudes, and Fourier amplitude ratios showed good agreement, but the Fourier phase parameters displayed a few discrepancies. To showcase the utility of the interpolators, the light curve of the RRab star EZ Cnc was generated and compared with the observed light curve from the *Kepler* mission. The reported distance to EZ Cnc was found to be in excellent agreement with the updated parallax measurement from Gaia EDR3. Our ANN interpolator provides a fast and efficient technique to generate a smooth grid of model light curves for a wide range of physical parameters, which is computationally expensive and time-consuming using stellar pulsation codes.

Key words: stars: variables: RR Lyrae – methods: data analysis — techniques: photometric

1 INTRODUCTION

RR Lyrae stars (RRLs) are old (≥ 10 Gyr), population II stars which are in the core helium-burning evolutionary phase of low-mass stars. They are located at the intersection of the horizontal branch (HB) and the instability strip (IS) in the HR diagram. They are low mass ($\sim 0.5M_{\odot}$), metal-poor stars which pulsate primarily in the fundamental mode (RRab) and in the first overtone (RRc) mode with periods ranging from ~ 0.2 d to 1.0 d (see e.g. Bhardwaj 2022). Many RRL variables are also classified as double mode pulsators (RRd) because they pulsate simultaneously in the fundamental and first overtone modes (Sandage et al. 1981; Jurcsik et al. 2015; Soszyński et al. 2017). RRLs exhibit a well defined period-luminosity-metallicity (PLZ) relation especially in the near-infrared bands (Longmore et al. 1986; Bono et al. 2001; Catelan et al. 2004; Sollima et al. 2006; Muraveva et al. 2015; Bhardwaj et al. 2021) and thus constitute as primary standard candles of the cosmic distance ladder. RRLs are also excellent probes to gain deeper insights into the theory of stellar evolution and pulsation (e.g. Marconi et al. 2015; Das et al. 2018; Marconi et al. 2018). RRLs are excellent tracers of the old stellar populations due to their age and have been detected in different

galactic (Vivas & Zinn 2006; Drake et al. 2013; Zinn et al. 2014; Pietrukowicz et al. 2015) and extra-galactic (Moretti et al. 2009; Soszyński et al. 2009; Fiorentino et al. 2010; Cusano et al. 2013) environments. They have also been identified in several globular clusters (Coppola et al. 2011; Di Criscienzo et al. 2011; Kuehn et al. 2013; Kunder et al. 2013).

Advancements in the theoretical modelling of stellar pulsation have made it possible to generate grids of light curves that correspond to a set of physical parameters of the variables using non-linear 1-D hydrodynamical codes, such as those described by Stellingwerf (1984); Bono et al. (1997, 1999); Marconi et al. (2015); De Somma et al. (2020, 2022). A grid of nonlinear convective hydrodynamical models was produced by Marconi et al. (2015) to study the pulsation properties of RRLs. This grid was created using horizontal-branch (HB) evolutionary models (for more information, see Pietrinferni et al. 2006, and its references) and takes into consideration different chemical compositions, luminosity levels, and stellar masses. The models were calculated using the hydrodynamical codes of Stellingwerf 1982 (updated later by Bono et al. 1998, 1999) and were based on the numerical and physical assumptions detailed in Bono et al. (1998, 1999) and Marconi et al. (2003, 2011).

Additionally, the radial stellar pulsations of Smolec & Moskalik (2008) available with the Modules for Experiments in Stellar Astrophysics (MESA Paxton et al. 2011, 2013, 2015, 2018, 2019), can

* E-mail: niteshchandra039@gmail.com

also be used to generate the light curves of radially pulsating variable stars.

The theoretical light curves generated from the available pulsation models have been utilized to investigate pulsation properties, derive PLZ relations, and provide a quantitative comparison with the observed light curves of Cepheid and RR Lyrae variables (Bono et al. 2000b; Keller & Wood 2002; Caputo et al. 2004; Marconi & Clementini 2005; Marconi & Degl'Innocenti 2007; Natale et al. 2008; Marconi et al. 2013, 2015, 2017; Bhardwaj et al. 2017a; Das et al. 2018; Ragosta et al. 2019; Bellinger et al. 2020; Das et al. 2020).

However, generating a model light curve from the given input parameters is still a computationally expensive problem, since it involves solving complex hydrodynamical equations. The processing time has been reduced significantly with modern computational facilities, but theoretical light curves for a fine grid of pulsation models covering the entire parameter space are still not feasible. A smooth grid of pulsation models of RR Lyrae and Cepheids is crucial to predict the physical parameters of these variables either through a model-fitting approach (Marconi et al. 2013) or using an automated comparison with observed light curves (Bellinger et al. 2020). Bellinger et al. (2020) obtained a catalogue of physical parameters for observed stars by applying machine-learning methods to the available Cepheid and RR Lyrae models, but the accuracy of physical parameters was limited due to the small number of models in the grid. These authors trained a neural network with light curve structure parameters like I and V band amplitudes, acuteness, skewness, and Fourier coefficients A_1, A_2, A_3 (see e.g., Deb & Singh (2009); Bhardwaj et al. (2015)) along with the period as input to predict the physical parameters of the model including mass (M), luminosity (L), radius (R), effective temperature (T_{eff}). The theoretical light curves computed by Marconi et al. (2015) & Das et al. (2018) were used for this analysis. They choose the input parameters based on the feature importance study using another ML algorithm, namely Random Forest (RF). The error on the derived parameters is estimated by perturbing the light curve parameters with random noise 100 times and passing them through the ANN.

In this study, we utilized a previously generated grid of models and employed modern automated methods to infer light curves. This was done by training an artificial neural network (ANN) using models from Marconi et al. (2015) and Das et al. (2018) to predict light curves based on a set of input parameters. This approach eliminates the need to solve complex time-dependent equations and can generate predictions much more efficiently.

The paper is organized as follows: The introduction of artificial neural networks and quantitative Fourier analysis is presented in Section 2. The input and observational datasets used for network training and comparison are described in Section 3. The tuning of the network architecture and training of the final interpolators in both I and V bands is discussed in Section 4. The validity of the trained interpolators is tested by comparing the newly generated model light curves with the ANN-predicted models in Section 4.5. In Section 5, the comparison of Fourier parameters between observed and predicted light curves of LMC and SMC in both I and V bands is discussed, and the distances to these galaxies are estimated. The applications of the trained interpolators are explored in Section 6, including a comparison of the observed and predicted V band light curve of a variable star (EZ Cnc) and the determination of its distance in Section 6.1. A smooth grid of light curve templates in I and V bands is generated using the ANN interpolators in Section 6.2. The results of the study are summarized in Section 7.

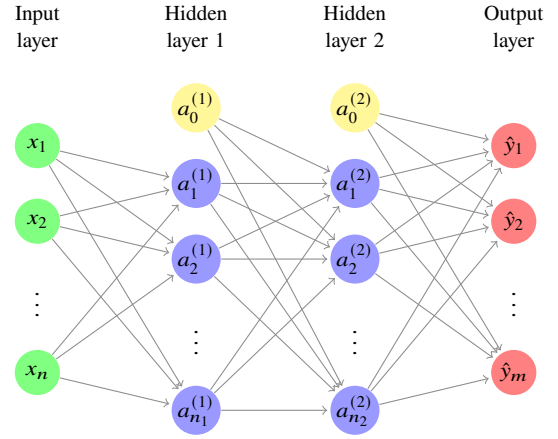


Figure 1. A representation of an artificial neural network with n inputs, two hidden layers having n_1 and n_2 neurons respectively and an output layer with m neurons. a_0 represents the bias terms in respective layers. The summation and non-linearity nodes are omitted for the sake of clarity.

2 METHODOLOGY

The theoretical grid of models can be thought of as being generated via a function f defined as

$$f(\mathbf{x}; \mathbf{w}) = [\text{light-curve}].$$

where \mathbf{x} is a combination of physical parameters of the stars, such as M, L, T_{eff}, X (hydrogen abundance ratio) and Z (metal abundance ratio), the period and a few other parameters including mixing length, radiative cooling, convective and turbulent flux parameters. Interested readers may refer to Marconi et al. (2015) and references therein for a better understanding of the input parameters required for the generation of light curves. Here \mathbf{w} are fitting parameters. If we assume that the function ‘ f ’ exists and is continuous and differentiable in parameter space: an ANN with one or more hidden layers can reproduce this function. Theoretically, Cybenko (1989); Hornik et al. (1989); Hornik (1991) showed that ANN with a non-linearly activated hidden layer, can approximate any continuous function with arbitrary accuracy when provided with enough neurons in the hidden layer. In addition, ANNs are flexible in the choice of architecture, and optimization algorithms, and are simple to implement. They also provide the possibility *transfer learning* and therefore is useful in the case of re-training the model with updated data.

2.1 Artificial Neural Network (ANN)

We employ the simplest neural network which is a feed-forward, fully-connected neural network. The smallest unit of the network, the neuron (or a perceptron) is a mathematical unit that calculates the weighted sum of all the neurons that are previously connected to it and feeds this output to all the neurons in the next layer after applying a non-linear activation function (σ) (see Fig. 1). The value of i^{th} neuron in k^{th} layer is calculated by,

$$a_i^{(k)} = \sigma^{(k)} \left(\sum_{j=0}^{n_{k-1}} w_{ij}^{(k-1)} a_j^{(k-1)} \right), \text{ for } 1 \leq i \leq n_k, \quad (1)$$

with,

$$a_0^{(k)} = 1, \quad (2)$$

here $\sigma^{(k)}$ is the activation function for the k^{th} layer, which is usually a nonlinear function. A few examples of widely used activation functions are rectified linear unit (or *relu*), sigmoid, and hyperbolic tangent (*tanh*). The weights of j^{th} neuron that is connected with i^{th} neuron in k^{th} layer are represented by $w_{ij}^{(k)}$ and are optimised to obtain a minimum (or maximum) value of a certain objective function during the training process. The weights are updated in an iterative process where in each iteration the errors obtained at the output layer are propagated back to the previous layers and thus making the network ‘better’ at every iteration. This algorithm was first conceptualised by Rumelhart et al. (1986) and is known as the backpropagation algorithm. This backpropagation algorithm is the backbone of modern stochastic gradient descent (SGD) algorithms (for a review of modern SGD algorithms, interested readers may go through Ruder 2016) that optimise the weights of the network based on the quantity that you want to optimise in order to train the network. Fig. 1 represents a schematic of a network with two hidden layers. We have assumed that at for input layer, $k \equiv 0$ and $\mathbf{a}^{(0)} \equiv \mathbf{x}$ and at the output layer $k \equiv L$ and $\mathbf{a}^{(L)} \equiv \hat{\mathbf{y}}$ ($\hat{\mathbf{y}}$ is the output of the network).

If the predicted and given absolute magnitude value of i^{th} model corresponding to j^{th} phase is \hat{y}_{ij} and y_{ij} , the mean square error (MSE) for the i^{th} model is calculated using:

$$\mathbb{E}_i \equiv (\text{MSE})_i = \frac{1}{N_s} \sum_{j=1}^{N_s} (y_{ij} - \hat{y}_{ij})^2, \quad (3)$$

where N_s is the total number of magnitude bin values for each model. The average MSE for all models in the grid can be calculated using:

$$\mathbb{E} \equiv \text{Avg. MSE} = \frac{1}{N} \sum_{i=1}^N (\text{MSE})_i = \frac{1}{N} \sum_{i=1}^N \left(\frac{1}{N_s} \sum_{j=1}^{N_s} (y_{ij} - \hat{y}_{ij})^2 \right). \quad (4)$$

where N is the total number of models in the training dataset. At every training iteration, for the simplest case of gradient descent learning, the weights are updated according to the following rule:

$$w_{ij}^{(k)} = w_{ij}^{(k)} - \eta \times \frac{\partial \mathbb{E}}{\partial w_{ij}^{(k)}} \quad (5)$$

where η is a scaling factor typically referred to as *learning parameter* that determines the size of the gradient descent steps. However, we used a modified version of the gradient descent algorithm known as the adaptive moment optimization algorithm (adam, Kingma & Ba 2014) where the learning parameter is also updated at each iteration to reach the minimum of the objective function efficiently.

2.2 Fourier parameters

The analysis of light curves using Fourier analysis has been discussed extensively in literature (Deb & Singh 2009; Bhardwaj et al. 2015; Das et al. 2018, and references therein). A Fourier series of sines is fitted to the theoretical and observed light curves and the parameters are deduced:

$$m = m_0 + \sum_{k=1}^N A_k \sin(2\pi k \Phi + \phi_k), \quad (6)$$

Here, A_k and ϕ_k are Fourier amplitude and phase coefficients, respectively, and Φ is the pulsation phase that ranges from 0 to 1, which is calculated using the following equation:

$$\Phi = \left[\frac{t - t_0}{P} \right] - \text{Int} \left[\frac{t - t_0}{P} \right], \quad (7)$$

here, t_0 is the epoch of maximum brightness, and P is the pulsation period of the star/model.

A_k and ϕ_k are used to calculate Fourier amplitude ratios (R_{k1}) and phase differences (ϕ_{k1}):

$$R_{k1} = \frac{A_k}{A_1}, \quad (8)$$

$$\phi_{k1} = \phi_k - k \phi_1, \quad (9)$$

where, $k > 1$ and $0 \leq \phi_{k1} \leq 2\pi$.

3 DATA

3.1 Training data

To train the neural network, we adopted the theoretical light curves of fundamental mode RR Lyrae (or RRab) models as described in Das et al. (2018). We used a total of 274 RRab light curves corresponding to a grid of physical parameters, out of which 166 were initially computed by Marconi et al. (2015) and the additional 108 by Das et al. (2018) using the same non-linear, time-dependent convective hydrodynamical models. The model light curves were generated in bolometric magnitudes and they were later transformed into Johnson Cousin photometric bands. A summary of theoretical RRab models is presented in Fig. 2. The models contain seven distinct chemical compositions ranging from $Z = 0.001$ to $Z = 0.02$, with a primordial He abundance, $Y = 0.245$, and a constant helium-to-metals enrichment ratio, $[\text{He}/\text{M}] = 1.4$ to replicate the initial helium abundance of the sun (Serenelli & Basu 2010). The pulsation models were constructed with different sets of stellar masses and luminosities, which were fixed according to detailed central He-burning horizontal-branch evolutionary models. The range of Z is broad enough for the comparison with the observed RR Lyrae stars in the satellite galaxies of the Milky Way, the Small Magellanic Cloud (SMC), and the Large Magellanic Cloud (LMC) (Clementini et al. 2003). A few models have pulsation periods greater than one day, thereby including the possibility of evolved RR Lyrae stars in the training data set. Out of the 274, six overlapping models were removed from the input dataset leaving 268 unique RRab models to train the ANN. The ANN models are described in detail in Section 4.

3.2 Observational data used for comparison

We used the observed light curves for a comparison with the ANN predicted light curves. Since the training light curves are in the Johnson Cousin filters bandpass, we need to have the observed light curves in the same filters. We used the I and V band light curves from the IV^{th} phase of the Optical Gravitational Lensing Experiment (OGLE¹) catalogue of RR Lyrae variables in LMC and SMC (Soszyński et al. 2016).

However, the observed magnitudes suffer from interstellar extinction and reddening due to the interaction of light with interstellar dust. We need to account for interstellar extinction and perform extinction corrections in magnitudes at a given wavelength. Using the positions (RA/Dec), we obtain the excess colour values, $E(V - I)$, for RRLs in the LMC and SMC from the reddening maps of Haschke

¹ <http://ogle.astrouw.edu.pl/>

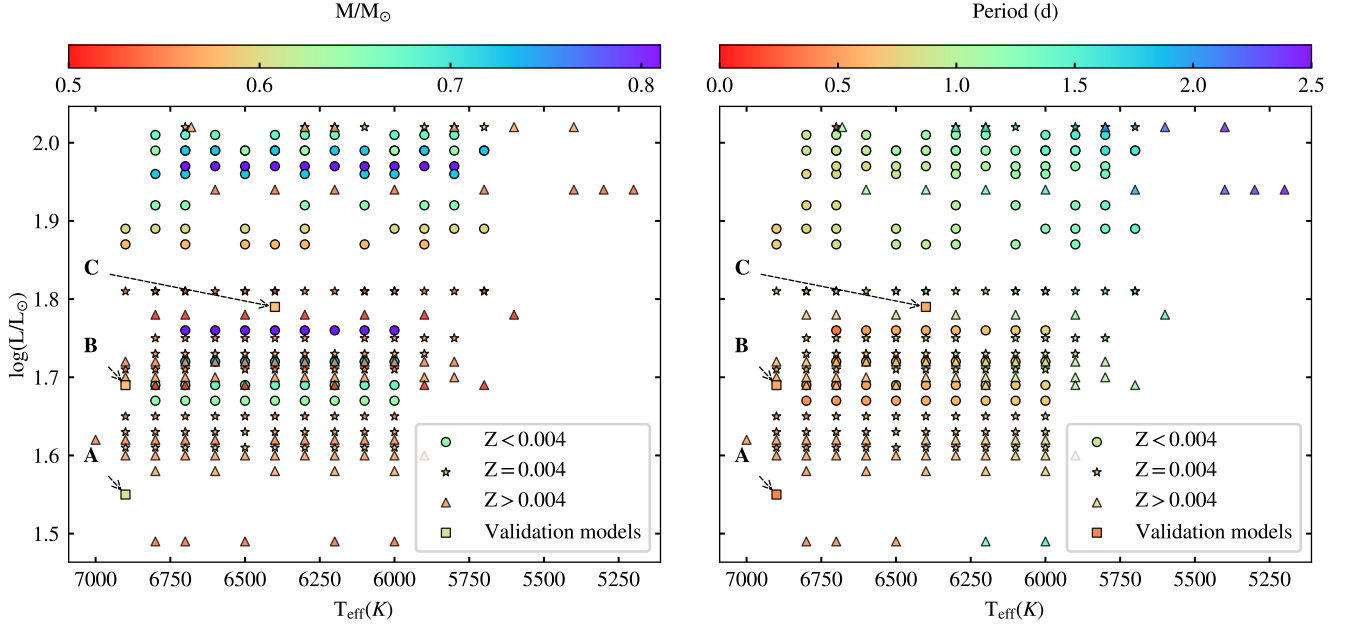


Figure 2. A visual representation of the input dataset of RRLs models described in Table 1. A few additional models were computed in this work for the validation of the trained ANN interpolators and are marked with **A**, **B**, and **C**

Table 1. A summary of 268 Fundamental mode RR Lyrae models.

Z	X	$\frac{M}{M_{\odot}}$	$\log \frac{L}{L_{\odot}}$	T _{eff} (K)	No. of RRab stars
0.02	0.71	0.51	1.69	5700 - 6800	6
			1.78	5600 - 6800	7
		0.54	1.49	6000 - 6800	5
			1.94	5200 - 6600	8
0.008	0.736	0.55	1.62	6000 - 7000	10
			1.72	5800 - 6900	12
			1.6	5900 - 6900	11
		0.56	1.7	5800 - 6900	10
			1.58	6000 - 6800	5
			2.02	5400 - 6680	6
0.004	0.746	0.53	1.81	5700 - 6800	7
			1.71	6000 - 6900	9
		0.56	1.81	5700 - 6900	13
			1.65	6000 - 6900	10
			1.75	5800 - 6800	10
		0.57	1.63	6000 - 6900	10
			1.73	5900 - 6800	10
			1.61	6000 - 6900	10
0.59	2.02	5700 - 6700	7		
	0.001	0.754	1.87	5900 - 6900	7
			1.67	6000 - 6800	9
1.99			5700 - 6800	10	
0.0006	0.7544	0.6	1.89	5700 - 6900	9
			1.69	6000 - 6800	9
		2.01	5800 - 6800	9	
0.0003	0.7547	0.65	1.92	5800 - 6800	6
			1.72	6000 - 6700	8
		1.99	5700 - 6700	10	
0.0001	0.7549	0.72	1.96	5800 - 6800	7
			1.76	6000 - 6700	8
		1.97	5800 - 6700	10	

et al. (2011). We apply extinction corrections using Schlegel’s list of conversion factors² -

$$A_V = 2.4 \times E(V - I) = 3.32 \times E(B - V), \quad (10)$$

and

$$A_I = 1.41 \times E(V - I) = 1.94 \times E(B - V). \quad (11)$$

4 ANN INTERPOLATOR FOR RR LYRAE MODELS

We used the ANN to interpolate the light curve for the input parameters within the grid. We built a feed-forward fully connected neural network and optimised its network architecture. The input layer of this network takes six parameters, which are:

$$\mathbf{x} \equiv \left[\frac{M}{M_{\odot}}, \log \left(\frac{L}{L_{\odot}} \right), T_{\text{eff}}, X, Z, \log(P) \right],$$

where M and L are the mass and luminosity of the model. T_{eff} is the effective temperature of the model in Kelvin. X and Z are the hydrogen and metal abundances of the model and the parameter P is the period in days. We have included the period as one of the inputs to facilitate ease for the user who might want to generate a model corresponding to a specific period.

The hydrodynamic models presented in Marconi et al. (2015) were generated using the same physical and numerical assumptions employed in earlier works, such as Bono et al. (1998, 1999) and Marconi et al. (2003, 2011). For instance, the radiative opacities used in their models were taken from the OPAL radiative opacities provided by the Lawrence Livermore National Laboratory (Iglesias & Rogers 1996), while the molecular opacities were obtained from Alexander & Ferguson (1994). Since the physical conditions, including the radiative

² <https://dc.zah.uni-heidelberg.de/mcextinct/q/cone/info>

Table 2. The hyperparameter search space for the network.

S.No.	Name of hyperparameter	Possible values
1	No. of hidden layers	[1, 2, 3]
2	No of neurons in one hidden layer	[16, 32, 64, 128]
3	Optimiser	‘adam’ (Kingma & Ba 2014)
4	Learning rate	$[10^{-2} - 10^{-4}]$ (log sampling)
5	Activation function	[‘relu’, ‘tanh’]
6	Weights initialisation	‘GlorotUniform’

and molecular opacities were kept constant, they were not considered as inputs to the ANN.

Each input parameter has a different numerical range, we need to transform each parameter to have the same numerical range as other input parameters. The input parameters are scaled in such a way that each input parameter has zero mean and unity standard deviation over the whole grid. At the output layer, we provide the corresponding (I or V band) light curve of the model which consists of the absolute magnitudes at a given series of phases. We have a total of 1000 magnitude values per model corresponding to phase values from 0 to 1 in steps of 0.001. We used a neural network that has one input layer with six input neurons, a few hidden layers (not more than three to keep the network small), and one output layer with 1000 output neurons containing the absolute magnitude corresponding to phase values between 0-1. We used a linear activation function ($\sigma^{(L)} \equiv 1$) between the last hidden layer and the output layer because we do not want to constrain the output values in any particular range. We have a total of 268 models, and hence the training matrix at the input layer has $[268 \times 6]$ and at the output layer is $[268 \times 1000]$.

4.1 Network Architecture and Hyperparameter optimisation

To have a generalised network that does not overfit/underfit the given dataset, we need to choose a suitable architecture (the number of hidden layers, the number of neurons in the hidden layer, activation functions) as well as the learning hyperparameters such as the loss optimization algorithm and parameters therein, etc (Elsken et al. 2019). Each individual hyperparameter has a significant role in the training process and a different value of a hyperparameter significantly affects the result of the training. However, there are no explicit ‘rules’ for selecting these attributes in such a way that the ANN model does not become trapped in a local solution. This is a crucial problem in the field of machine learning (Guo et al. 2008).

The choice of architecture and hyperparameters usually depends on the intuition of the expert and hand tuning. Typically, the trial-and-error approach like grid search and random search (Bergstra & Bengio 2012) is used to determine these characteristics. We created a grid of possible hyperparameters by choice and intuition that we gained working with the dataset, which is tabulated in Table 2. Out of various possible combinations, we chose a set of 100 hyperparameter combinations at random. We then trained the network for fixed 1000 epochs with the L2 norm (MSE) as the objective function using the ‘‘adaptive moment stochastic gradient descent (or adam: Kingma & Ba 2014)’’ algorithm with a default batch size of 32 samples. The network architecture was optimised using the I band light curves. For this procedure, we utilised Keras tuner (O’Malley et al. 2019).

We show the result of the top 10 performing network architectures in Table 3. We observe that a network with 3 hidden layers with 64, 128, 128 neurons in successive hidden layers with an initial learning rate(η) $\sim 1.8 \times 10^{-3}$, reaches the minimum MSE in 1000 epochs of learning. Fig. 3 depicts the learning curves for the top-10 network architectures listed in Table 3.

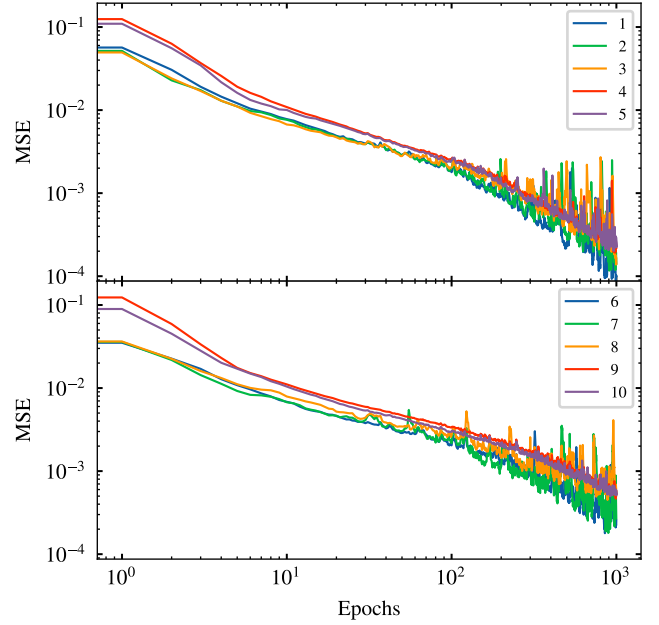


Figure 3. Training curves of the network architectures described in Table 3. We seek such an architecture that converges to the minimum rapidly in the first 1000 epochs. We find that the network with architecture 1 reaches the minimum fastest.

4.2 Training of the I band Interpolator

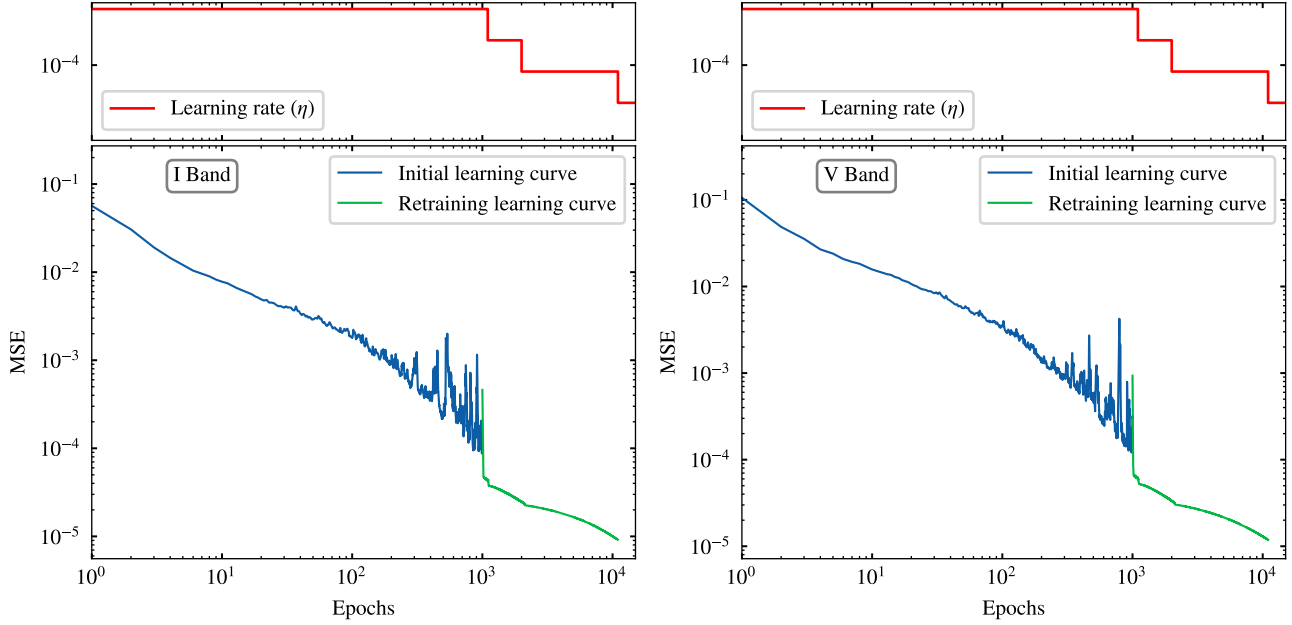
To construct the final interpolator for the I band, we used the architecture that performed best in the architecture optimization step, i.e., architecture 1. In the previous step, we note that the training loss (MSE) decreases globally at large epochs, but the individual updates are quite big and the loss oscillates rapidly (see Fig. 3). High learning rates cause such oscillations in the learning curve. The oscillations can be reduced by reducing the learning parameter; however, we don’t want to start the training with a low η because it impairs the performance of the network (see the comparison between architecture no. 1 and 4: the low learning rate causes the network to return comparatively higher MSE). Hence, we employ ‘piece-wise decay’ of the learning rate to mitigate these oscillations of loss at higher epochs. To do this, we begin with the best-performing network of the previous step and re-train it with a decreasing learning rate. We reduce the current learning rate by dividing it by a constant number (δ) when the epoch crosses successive powers of 10. We chose $\delta = 5$, based on the intuition we gained after experimenting with a few values of δ . This guarantees that the loss diminishes gradually as the training epochs increase. We trained this network for 11,000 epochs and obtained a minimum MSE of 9.07×10^{-6} . The final learning curve (epoch vs loss curve) is shown in Fig. 4 along with the learning parameter (η) in the top panel. This final network is adopted as the I band ANN interpolator for fundamental mode RR Lyrae models.

4.3 Training of the V band Interpolator

The problem of training the network for interpolating the light curve in a different band is a similar problem that we tackled in the previous step and hence we used the same network architecture that performed best during the I band interpolator training, to train the V band interpolator. We started the training with a neural network with 3 hidden

Table 3. The performance of different neural network architectures trained with the different combinations of hyperparameters.

Architecture No.	No. of Hidden Layers	Hlayer 1	Hlayer 2	Hlayer 3	Activation	Learning Rate(η)	Min MSE
1	3	64	128	128	relu	1.7941×10^{-3}	8.7585×10^{-5}
2	3	32	64	128	relu	2.5664×10^{-3}	1.3403×10^{-4}
3	3	64	32	128	relu	3.3848×10^{-3}	1.8869×10^{-4}
4	3	64	128	128	relu	8.2402×10^{-4}	2.1454×10^{-4}
5	3	128	64	128	relu	1.1231×10^{-3}	2.1862×10^{-4}
6	2	128	128	–	relu	3.2495×10^{-3}	2.5605×10^{-4}
7	3	32	32	128	relu	6.1855×10^{-3}	2.7093×10^{-4}
8	3	32	128	32	relu	6.9244×10^{-3}	4.3660×10^{-4}
9	2	128	128	–	relu	8.5086×10^{-4}	4.4778×10^{-4}
10	2	64	128	–	relu	1.2916×10^{-3}	4.6174×10^{-4}

**Figure 4.** The learning curve for both the *I* and *V* band is shown in the respective blocks along with the learning rate parameter. The blue curve in each plot represents the training curve till the initial 1000 epochs trained with the best-performing network architecture obtained using random search. We then transfer the trained weights and re-train the network with piece-wise decay of the learning rate. The orange curve represents the training curve in this phase.

layers which contain 64, 128, 128 neurons respectively. We started to train the network with the same ‘adam’ optimization algorithm with the same initial learning rate parameter ($\eta = 1.7941 \times 10^{-3}$). After the initial training for 1000 epochs, we encounter the same problem of loss oscillations, and hence we treat the learning rate in the same manner as we did in the case of the *I* band interpolator. The learning curve for the *V* band interpolator along with the adopted learning rate parameter is shown in the right panel of Fig. 4.

4.4 Training statistics for interpolators

We calculated the statistics between the original model light curves and the ANN generated/predicted light curves. We determined the average mean squared error (MSE), mean absolute error (MAE) and the coefficient of determination (R^2) between the original and predicted magnitude values for a quantitative comparison (Steel et al. 1960; Draper & Smith 1998; Glantz & Slinker 2001). We have already discussed the MSE in Section 2.1. The MAE for one model is

defined by:

$$\text{MAE} = \frac{1}{N_s} \sum_{j=1}^{N_s} |y_j - \hat{y}_j|.$$

and R^2 is defined by:

$$R^2 = 1 - \frac{\sum (y_j - \hat{y}_j)^2}{\sum (y_j - \bar{y})^2}.$$

where y_j and \hat{y}_j is the original and predicted magnitude value corresponding to the j^{th} phase and $\bar{y} = \frac{\sum y_j}{N_s}$. N_s is the total number of sample points for the light curve. We quote the average of each quantity over the whole dataset.

The training statistics for both *I* and *V* bands are given in Table 4. For the *I* band interpolator, we achieve a minimum MSE of $\sim 9.076 \times 10^{-6}$, with corresponding MAE of $\sim 2.162 \times 10^{-3}$ and $R^2 \sim 0.9987$. For the *V* band interpolator, we achieve a minimum MSE of 1.175×10^{-5} , with corresponding MAE of $\sim 2.503 \times 10^{-3}$ and $R^2 \sim 0.9994$.

Table 4. The statistics of the interpolators on training data.

Band	No. of Models	MSE	MAE	R^2
I	268	9.076×10^{-6}	2.162×10^{-3}	0.99879
V	268	1.175×10^{-5}	2.503×10^{-3}	0.99940

Table 5. The statistics of the interpolators on validation data.

Band	No. of Models	MSE	MAE	R^2
I	3	2.316×10^{-3}	3.375×10^{-2}	0.95123
V	3	2.658×10^{-3}	3.5001×10^{-2}	0.96911

4.5 Validation of Interpolators

To validate our method, we computed three additional models using the same hydrodynamical code and compared the light curves predicted by the ANN with the ones obtained from these models. The comparison between the ANN generated light curves and the model light curves in *I* and *V* bands can be seen in Figs 5 and 6 respectively. The physical parameters for the validation models were selected from a relatively scarce parameter space. The results, shown in Table 5, indicate that the light curves predicted by the ANN are consistent with the model light curves. The validation models produced an average mean squared error (MSE) of 2.316×10^{-3} in the *I* band, corresponding to an average R^2 value of 0.95, and an MSE of 2.658×10^{-3} in the *V* band, corresponding to an average R^2 value of 0.97. This agreement between the ANN generated light curves and the new model light curves demonstrates the validity of our ANN models and confirms that they can be used to generate light curves in both *V* and *I* bands.

5 COMPARISON OF OBSERVED LIGHT CURVES WITH THE GENERATED LIGHT CURVES USING INTERPOLATORS

Theoretical models are used to complement observational data and are tested on the observed light curves of stars for which the physical parameters are already known. To accurately determine the physical parameters of RR Lyrae stars, a detailed spectroscopic and photometric analysis is often required (see e.g. Wang et al. 2021). However, in some cases, it is not feasible to obtain spectroscopic measurements of such stars, so data-driven methods are necessary to infer their physical properties. One such method is presented in the study by Bellinger et al. (2020). The authors have predicted the physical parameters (mass, luminosity, effective temperature, and radius) of stars in the LMC and SMC using the OGLE-IV survey, which provides the *I* and *V* band light curves of various types of variable stars, including RR Lyrae. The authors used an ANN to derive the parameters by training it with the relationship between light-curve structure (including amplitudes, acuteness, skewness, and coefficients of the Fourier series) and physical parameters of the models. By comparing the ANN generated light curve based on these parameters to the observed light curves, the validity of the derived parameters can be evaluated. This comparison was done by comparing the amplitudes, Fourier parameters, and their distribution with the period of pulsation of the ANN generated light curves to the observed light curves. We stress that the ANN used by Bellinger et al. (2020) to estimate the physical parameters based on the light curves and the one we use to predict the light curves based on the physical parameters, were trained on the exact same set of hydrodynamical models.

The ANN model requires a total of six input parameters:

$\left[\frac{M}{M_{\odot}}, \log \left(\frac{L}{L_{\odot}} \right), T_{\text{eff}}, X, Z, \log(P) \right]$ to predict the light curve. We used the ‘Lomb-Scargle’ algorithm (Lomb 1976; Scargle 1982) to determine the period from the observed magnitudes in un-evenly spaced observations and we calculated the *Z* values for the Bellinger et al. (2020) stars from photometric metallicities ($[\text{Fe}/\text{H}]$) provided by Skowron et al. (2016). The steps for transformation from $[\text{Fe}/\text{H}]$ to *Z* are provided as follows: If the composition of a star is solar scaled, the following relation holds (Piersanti, L. et al. 2007),

$$[\text{Fe}/\text{H}] = \log(Z/X)_{\star} - \log(Z_{\odot}/X_{\odot}). \quad (12)$$

For Sun, we adopted $X_{\odot} = 0.7392$, $Y_{\odot} = 0.2486$, $Z_{\odot} = 0.0122$ from Asplund et al. (2005). Also, we fixed $Y = 0.245$ for the RRL stars and determined the values of *X* and *Z* for each star by cross-matching Bellinger et al. and Skowron et al..

We managed to compile the required input parameters for the 7789 RRab stars of LMC, and 676 stars of SMC. With the adopted input parameters we generated the light curves and determined the peak-to-peak amplitude (*A*) and Fourier parameters ($R_{21}, R_{31}, R_{41}, R_{51}, \phi_{21}, \phi_{31}, \phi_{41}, \phi_{51}$) by fitting a Fourier series defined by equation 6 with $N = 5$.

Fig. 7 displays the peak-to-peak amplitudes for the observed and predicted light curves of RR Lyrae in the Magellanic Clouds in the *I* and *V* band, respectively. We find that the predicted amplitudes are in good agreement with the observed amplitudes of RR Lyrae variables. For the LMC variables, there seem to be two amplitude sequences for the longer period RRab ($\log P \gtrsim -0.22$) stars. The theoretical models reproduce relatively larger amplitudes for Cepheids and RR Lyrae than the observations in optical bands (Bhardwaj et al. 2017b; Das et al. 2018), and the higher amplitude sequence can be attributed to this systematic in the models for specific mass-luminosity levels. The discrepancy is known to be related to the treatment of super adiabatic convection as the considered pulsation models, and Marconi et al. 2015, assume a single value for the mixing length parameter that is used in the code to close the nonlinear equation system. Nevertheless, the majority of the predicted and the observed amplitudes are in good agreement.

5.1 Comparison of the Fourier parameters of models with observations

Fig. 8 and Fig. 9 display the Fourier parameters of the predicted and observed light curves of LMC and SMC in both *I* and *V* bands respectively. For RRab in both the clouds, the Fourier amplitude ratio values from the predicted light curves agree well with the observations, but the predicted phase parameters show a systematic offset and a larger dispersion. We also note that phase parameters exhibit a strong correlation with the metallicity (Jurcsik & Kovacs 1996; Nemeč et al. 2013; Mullen et al. 2021) and such systematic may also arise from the uncertainties in the input photometric metallicities.

It should be noted that the predicted physical parameters for these variables from Bellinger et al. (2020) are not highly precise, and their accuracy is limited by the lack of a fine grid of models. The derived physical parameters are used to generate the light curve using the trained interpolators. A good match between ANN generated and observed light curves is expected since the same theoretical models were employed to train the ANN used by us and the ANN trained by Bellinger et al. (2020). However, it should be noted that the phase parameters were not included in the training input used to derive the physical parameters in Bellinger et al. (2020). Despite including convection in the hydrodynamical models, it remains difficult to match the observed Fourier phase parameters of RRLs with theoretical models (Feuchtinger 1999; Paxton et al. 2019). Comparative

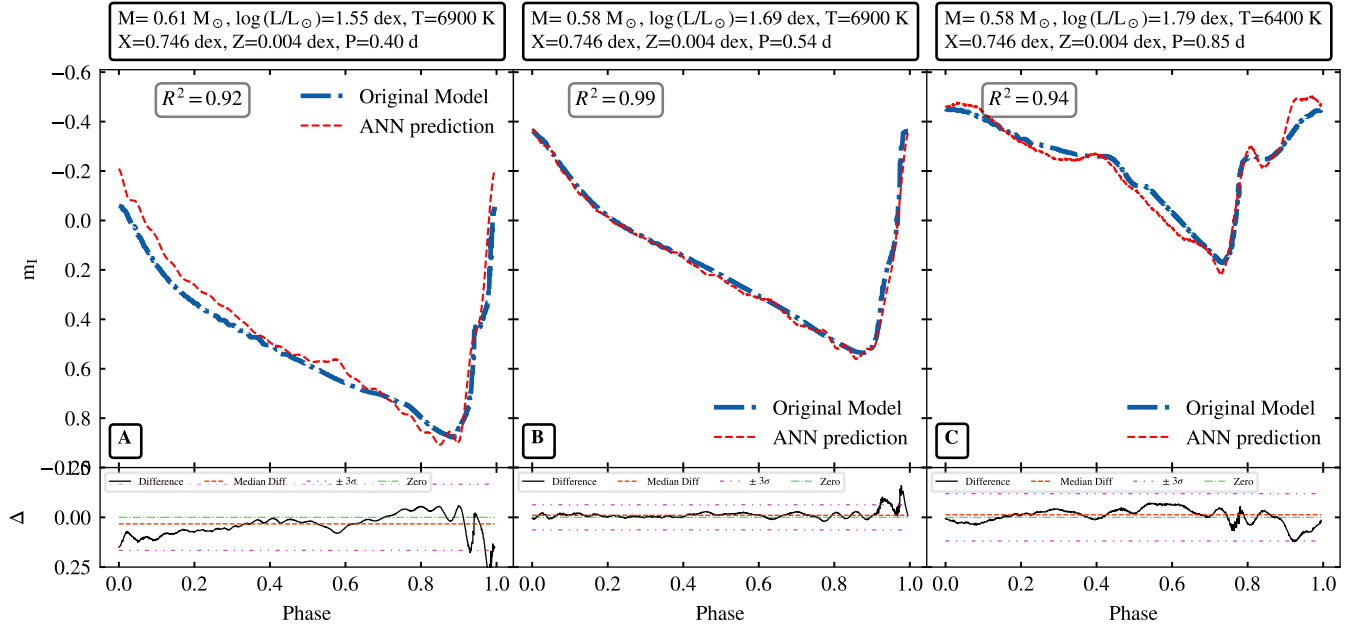


Figure 5. The comparison of the original I band light curve, represented by the blue background line, and the ANN reconstructed light curve, shown as the foreground red line, is displayed for three models. These light curves were generated using the same hydrodynamical code for validation purposes. The input parameters for each light curve plot can be found in the upper panel. The difference between the two light curves is depicted in the bottom panel with a black line, with the magenta line representing the 3σ bounds and the green line indicating the mean deviation between the predicted and actual light curves. The goodness of fit parameter R^2 is also calculated for each plot and displayed.

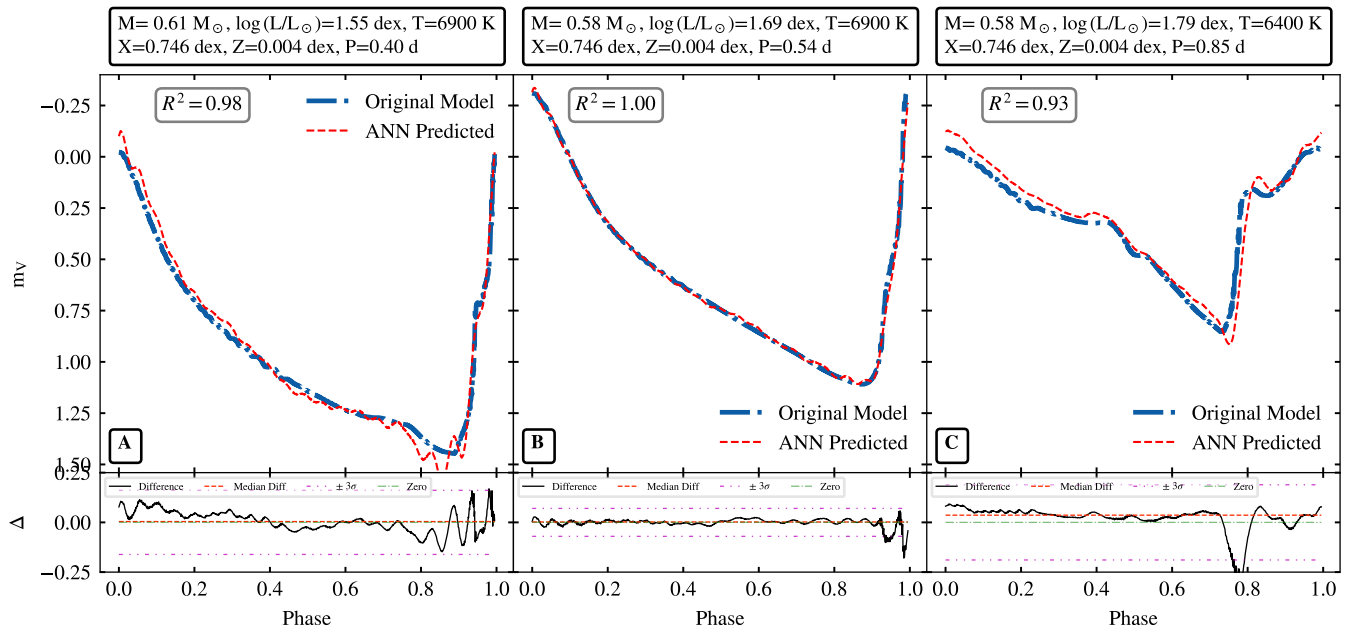


Figure 6. Same as Fig. 5 but for V band.

studies of the theoretical RR Lyrae models generated by [Marconi et al. \(2015\)](#) with the observations show an offset in the value of Fourier phase parameters. The models predict higher Fourier phases than the observations ([Das et al. 2018](#)). The same effect gets propagated through the ANN, and the phase parameters derived from the

light curves generated using the ANN interpolator are slightly higher than the observed values for both LMC and SMC.

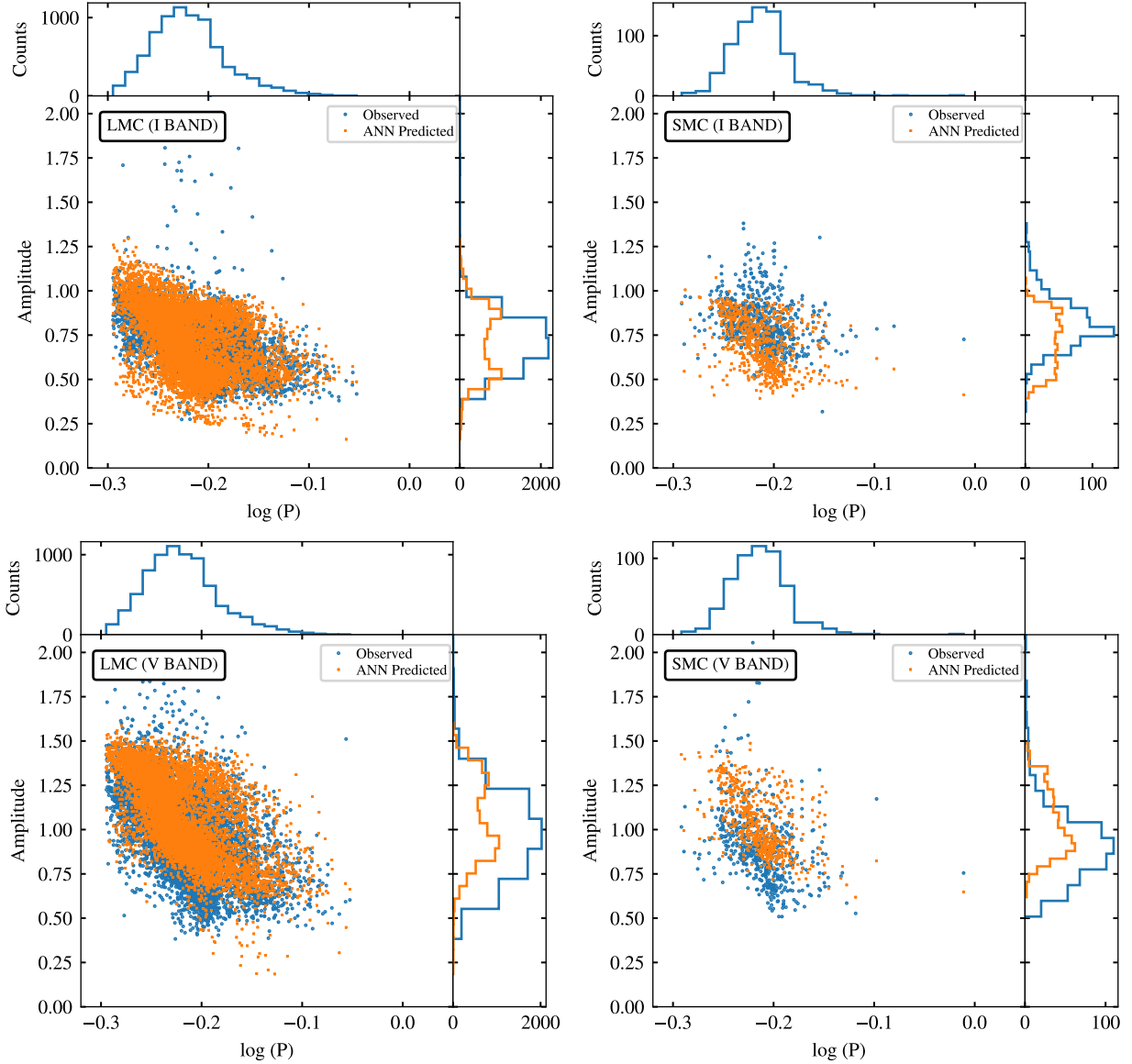


Figure 7. Peak to peak amplitude against $\log(P)$ for Observed and ANN generated light curves of LMC and SMC stars. The extended panel in each plot shows the histograms of periods on the x-axis and amplitudes on the y-axis.

5.2 Distance modulus to the Magellanic Clouds

The predicted light curves generated by the ANN model can be employed to estimate the distance modulus of the Magellanic Clouds. We adopted the reddening-independent Wesenheit index (Madore 1982) to determine the distances, which is defined as $W = I - 1.55 \times (V - I)$. The Wesenheit index is a commonly used method for estimating distances (Soszyński et al. 2018). We calculated the Wesenheit index-based distance moduli ($W_m - W_M$) to estimate the distances to the Magellanic Clouds.

The distance moduli of individual RRab stars in the Magellanic Clouds are computed based on the Wesenheit index and are depicted in Fig. 10. By removing outliers beyond $5\text{-}\sigma$, the average distance modulus of RRab stars in the LMC and SMC are determined to be $\mu_{\text{LMC}} = 18.567 \pm 0.135$ mag and $\mu_{\text{SMC}} = 18.93 \pm 0.17$ mag respectively. These estimates are consistent with previously published distances of the Magellanic Clouds based on eclipsing binaries ($\mu_{\text{LMC}} = 18.476 \pm 0.024$ mag, and $\mu_{\text{SMC}} = 18.95 \pm 0.07$ mag;

Graczyk et al. 2014; Pietrzyński et al. 2019). It is important to note that the methodology employed in this study does not presuppose any prior period-magnitude relationship, and the obtained distance estimates are simply a result of accurately predicted light curves of observed stars in the Magellanic Clouds.

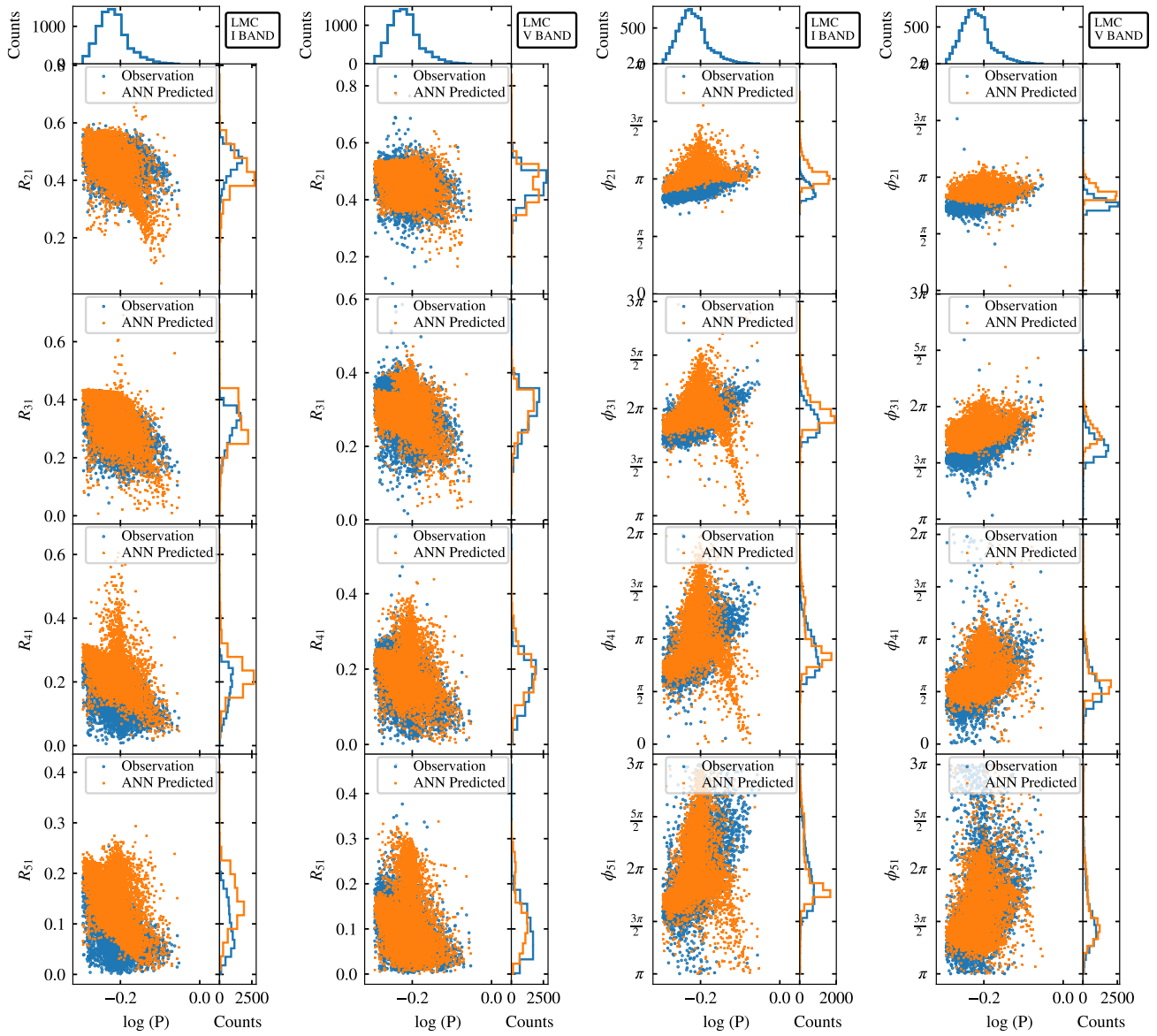


Figure 8. This plot displays the comparison between the Fourier amplitude ratios and phase differences of the light curves predicted by ANN and the actual observations for LMC, in both the *I* and *V* bands, as a function of period.

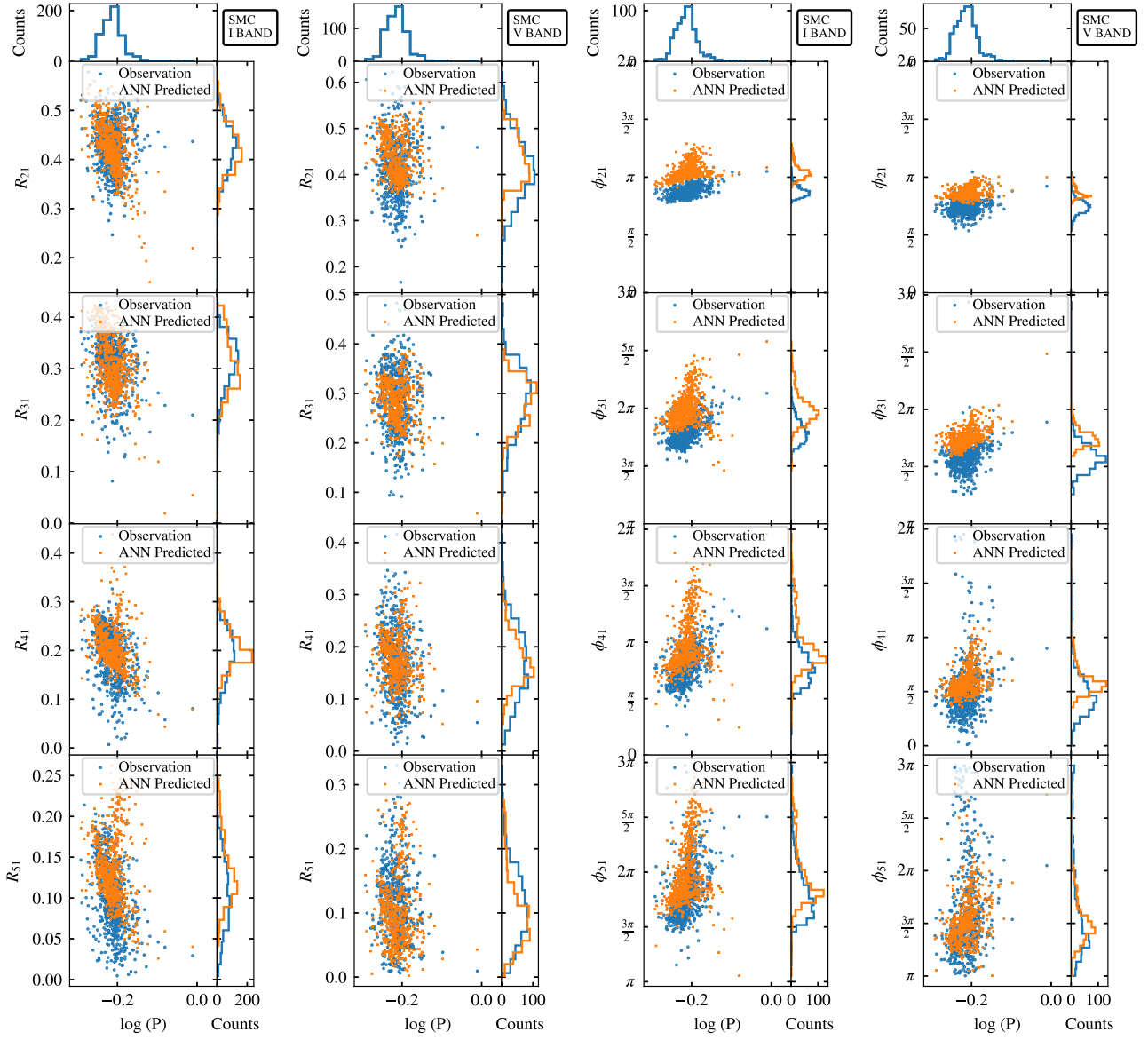


Figure 9. Same as Fig. 8 but for SMC.

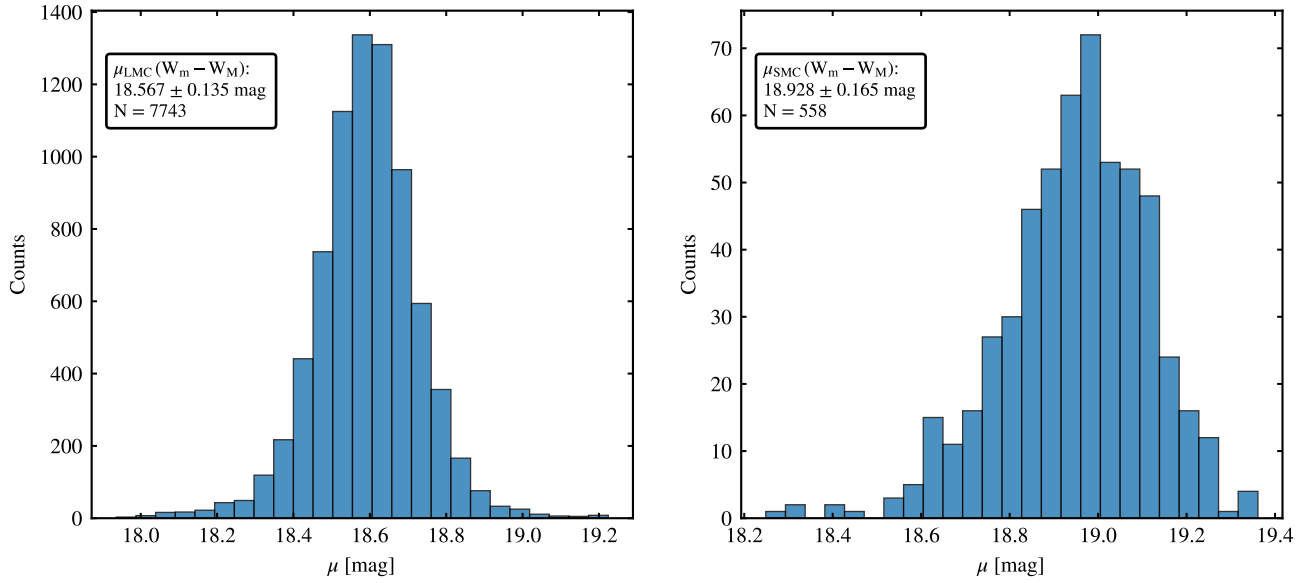


Figure 10. The graph presents a histogram of the distance modulus calculated through the Wesenheit index. The left side shows the distribution of the distance modulus for stars in the Large Magellanic Cloud, while the right side displays the distribution for the Small Magellanic Cloud. In each plot, on the top left corner, a box lists the weighted average distance modulus and the number of stars (N) considered after outliers were removed using a 5σ threshold in sigma clipping.

Table 6. The table displays the calculated ANN predicted mean magnitudes, amplitudes, and Fourier parameters, along with the observations. The complete table can be accessed online in a machine-readable format.

OGLE ID	λ	M_{bol}	$\log\left(\frac{L}{L_{\odot}}\right)$	T_{eff} (K)	X (dex)	Z (dex)	P (d)	m_{obs} (mag)	M_{ANN} (mag)	A_{obs} (mag)	A_{ANN} (mag)	$R_{21_{\text{obs}}}$	$R_{21_{\text{ANN}}}$	$\phi_{21_{\text{obs}}}$	$\phi_{21_{\text{ANN}}}$	$R_{31_{\text{obs}}}$	$R_{31_{\text{ANN}}}$	$\phi_{31_{\text{obs}}}$	$\phi_{31_{\text{ANN}}}$	$R_{41_{\text{obs}}}$	$R_{41_{\text{ANN}}}$	$\phi_{41_{\text{obs}}}$	$\phi_{41_{\text{ANN}}}$	$R_{51_{\text{obs}}}$	$R_{51_{\text{ANN}}}$	$\phi_{51_{\text{obs}}}$	$\phi_{51_{\text{ANN}}}$
LMC-0008	I	0.605±0.054	1.778±0.044	6490±110	0.753971	0.001029	0.7877152±3.1e-06	18.679±0.002	-0.155±0.001	0.462±0.076	0.663±0.234	0.385±0.024	0.419±0.005	3.257±0.078	3.267±0.015	0.23±0.024	0.119±0.005	0.334±0.114	0.173±0.042	0.046±0.023	0.045±0.005	3.834±0.506	2.089±0.105	0.024±0.024	0.024±0.005	1.518±0.946	3.454±0.199
LMC-0010	I	0.676±0.059	1.667±0.044	6380±110	0.754428	0.000572	0.5940743±1.6e-06	18.819±0.002	0.094±0.001	0.765±0.095	0.563±0.166	0.447±0.026	0.397±0.001	2.858±0.068	3.437±0.029	0.345±0.024	0.275±0.009	5.918±0.096	0.336±0.043	0.178±0.023	0.213±0.009	2.78±0.159	3.81±0.056	0.057±0.022	0.16±0.009	5.101±0.436	0.88±0.073
LMC-00027	I	0.714±0.056	1.828±0.045	6270±110	0.753610	0.001390	0.7938821±3e-06	18.507±0.002	-0.294±0.001	0.551±0.065	0.438±0.221	0.426±0.023	0.206±0.006	3.157±0.068	3.322±0.028	0.244±0.023	0.13±0.005	0.424±0.109	3.758±0.045	0.111±0.023	0.103±0.005	3.617±0.21	0.402±0.057	0.07±0.022	0.107±0.005	1.601±0.334	3.693±0.057
LMC-00072	I	0.693±0.055	1.698±0.045	6360±110	0.754293	0.000707	0.6261742±2e-06	18.886±0.002	0.027±0.001	0.558±0.068	0.554±0.169	0.415±0.021	0.373±0.011	2.923±0.062	3.44±0.031	0.28±0.021	0.275±0.01	6.155±0.09	0.187±0.044	0.144±0.022	0.198±0.01	3.379±0.156	3.687±0.06	0.042±0.019	0.14±0.009	0.744±0.481	0.771±0.082
LMC-00082	I	0.665±0.058	1.715±0.043	6690±110	0.754716	0.000284	0.565446±8e-07	18.741±0.003	0.082±0.001	0.808±0.072	0.905±0.321	0.465±0.02	0.474±0.006	2.623±0.055	3.018±0.016	0.377±0.02	0.395±0.006	5.485±0.074	5.776±0.022	0.275±0.019	0.252±0.006	2.292±0.101	2.249±0.031	0.151±0.018	0.175±0.006	5.466±0.154	5.248±0.042
SMC-0001	I	0.595±0.057	1.661±0.043	6640±110	0.754758	0.000242	0.588145±9e-07	19.065±0.003	0.166±0.001	0.899±0.084	0.871±0.184	0.444±0.019	0.462±0.005	2.643±0.052	3.069±0.013	0.341±0.018	0.382±0.005	5.359±0.072	6.153±0.018	0.249±0.017	0.222±0.005	1.968±0.098	2.591±0.027	0.165±0.017	0.13±0.005	5.01±0.131	5.583±0.042
SMC-0002	I	0.581±0.054	1.604±0.043	6420±100	0.754461	0.000539	0.594794±1.9e-06	19.011±0.003	0.202±0.001	0.689±0.071	0.519±0.211	0.441±0.028	0.396±0.009	2.837±0.077	3.545±0.027	0.304±0.027	0.219±0.009	5.906±0.114	0.232±0.047	0.148±0.026	0.253±0.009	3.073±0.202	3.413±0.048	0.091±0.026	0.201±0.009	0.351±0.303	0.355±0.06
SMC-0003	I	0.648±0.05	1.723±0.044	6570±110	0.754293	0.000707	0.6506795±3.3e-06	19.158±0.002	0.019±0.001	0.911±0.24	0.797±0.183	0.323±0.027	0.444±0.005	2.938±0.099	3.186±0.015	0.179±0.027	0.344±0.005	6.173±0.168	6.072±0.02	0.052±0.026	0.176±0.005	3.502±0.52	2.67±0.034	0.018±0.027	0.086±0.005	0.495±1.459	5.644±0.062
SMC-0008	I	0.697±0.05	1.675±0.042	6270±100	0.754268	0.000732	0.6328767±2.1e-06	19.154±0.002	0.052±0.001	0.788±0.103	0.5±0.145	0.416±0.027	0.407±0.012	2.911±0.078	3.625±0.036	0.281±0.026	0.305±0.012	6.175±0.115	0.71±0.051	0.109±0.026	0.264±0.012	3.156±0.247	4.485±0.063	0.048±0.024	0.208±0.012	0.595±0.535	1.672±0.079
SMC-0011	I	0.669±0.051	1.697±0.042	6530±100	0.754651	0.000349	0.5957643±1.8e-06	19.17±0.003	0.075±0.001	0.962±0.134	0.738±0.189	0.359±0.029	0.419±0.005	2.649±0.094	3.171±0.015	0.268±0.029	0.321±0.005	5.682±0.129	6.065±0.021	0.149±0.028	0.194±0.005	2.501±0.209	2.779±0.032	0.099±0.028	0.109±0.005	5.522±0.303	5.897±0.052
LMC-00008	V	0.605±0.054	1.778±0.044	6490±110	0.753971	0.001029	0.7877152±3.1e-06	19.419±0.013	0.384±0.001	0.583±0.079	0.828±0.377	0.377±0.089	0.339±0.005	2.798±0.256	2.752±0.018	0.179±0.071	0.193±0.005	5.868±0.557	5.965±0.031	0.105±0.065	0.018±0.005	3.083±0.883	1.997±0.287	0.096±0.072	0.032±0.005	0.003±0.906	0.847±0.163
LMC-00010	V	0.676±0.059	1.667±0.044	6380±110	0.754428	0.000572	0.5940743±1.6e-06	19.466±0.012	0.659±0.002	0.774±0.043	0.87±0.19	0.408±0.076	0.399±0.01	2.386±0.21	2.842±0.029	0.375±0.073	0.276±0.01	5.167±0.271	5.583±0.043	0.299±0.079	0.18±0.009	1.701±0.34	2.103±0.063	0.099±0.071	0.142±0.009	4.029±0.832	5.161±0.079
LMC-00072	V	0.693±0.055	1.698±0.045	6360±110	0.754293	0.000707	0.6261742±2e-06	19.563±0.011	0.588±0.002	0.672±0.039	0.833±0.181	0.424±0.067	0.388±0.01	2.429±0.175	2.867±0.031	0.252±0.056	0.257±0.01	5.347±0.279	5.576±0.047	0.17±0.061	0.175±0.01	2.014±0.368	2.165±0.067	0.094±0.064	0.132±0.01	5.655±0.634	5.127±0.086
LMC-00079	V	0.623±0.055	1.66±0.044	6590±110	0.754575	0.000425	0.5647915±1.4e-06	19.602±0.018	0.076±0.001	0.858±0.044	1.141±0.31	0.57±0.117	0.458±0.003	2.474±0.305	2.596±0.009	0.34±0.095	0.321±0.003	5.308±0.443	5.404±0.013	0.293±0.105	0.18±0.003	1.712±0.563	1.733±0.021	0.276±0.072	0.079±0.003	4.812±0.714	4.646±0.041
LMC-00082	V	0.665±0.058	1.715±0.043	6690±110	0.754716	0.000284	0.565446±8e-07	19.314±0.019	0.58±0.002	1.001±0.035	1.343±0.306	0.393±0.077	0.49±0.006	2.278±0.258	2.625±0.015	0.276±0.085	0.328±0.005	4.938±0.34	5.176±0.022	0.201±0.071	0.234±0.005	1.496±0.528	1.339±0.03	0.123±0.071	0.15±0.005	3.158±0.786	4.025±0.042
SMC-0001	V	0.595±0.057	1.661±0.043	6640±110	0.754758	0.000242	0.588145±9e-07	19.594±0.014	0.667±0.001	1.052±0.074	1.25±0.301	0.385±0.052	0.489±0.003	2.04±0.184	2.612±0.009	0.342±0.06	0.333±0.003	4.461±0.209	5.602±0.013	0.277±0.055	0.189±0.003	0.997±0.272	1.841±0.02	0.091±0.047	0.081±0.003	3.5±0.492	4.666±0.041
SMC-0002	V	0.581±0.054	1.604±0.043	6420±100	0.754461	0.000539	0.594794±1.9e-06	19.615±0.007	0.797±0.002	1.014±0.143	0.767±0.254	0.484±0.048	0.408±0.011	2.48±0.097	2.681±0.032	0.252±0.038	0.23±0.01	5.515±0.184	5.455±0.054	0.127±0.035	0.176±0.01	2.102±0.34	2.025±0.071	0.107±0.039	0.14±0.01	5.791±0.366	4.528±0.089
SMC-0003	V	0.648±0.05	1.723±0.044	6570±110	0.754293	0.000707	0.6506795±3.3e-06	19.767±0.004	0.539±0.001	0.794±0.152	1.041±0.334	0.331±0.03	0.447±0.005	2.568±0.117	2.612±0.013	0.22±0.03	0.309±0.005	5.338±0.168	5.413±0.02	0.077±0.028	0.149±0.005	2.339±0.413	1.503±0.035	0.046±0.028	0.053±0.004	0.287±0.617	4.14±0.087
SMC-0008	V	0.697±0.05	1.675±0.042	6270±100	0.754268	0.000732	0.6328767±2.1e-06	19.742±0.003	0.639±0.002	0.986±0.154	0.943±0.241	0.422±0.024	0.424±0.014	2.436±0.068	3.006±0.04	0.227±0.022	0.359±0.014	5.445±0.117	6.068±0.053	0.116±0.022	0.269±0.013	2.048±0.211	2.899±0.071	0.012±0.022	0.238±0.013	5.254±1.699	6.175±0.085
SMC-0011	V	0.669±0.051	1.697±0.042	6530±100	0.754651	0.000349	0.5957643±1.8e-06	19.81±0.008	0.605±0.001	1.054±0.102	1.043±0.251	0.436±0.037	0.426±0.005	2.048±0.115	2.647±0.013	0.215±0.036	0.284±0.004	4.605±0.201	5.3±0.02	0.102±0.036	0.17±0.004	0.84±0.357	1.685±0.03	0.05±0.035	0.081±0.004	2.629±0.718	4.565±0.057

Table 7. The stellar parameters of EZ Cnc (EPIC 212182292) adopted from Wang et al. (2021)

Parameter	Value
Mass (M)	$0.48 \pm 0.03 M_{\odot}$
Luminosity (L)	$42 \pm 2 L_{\odot}$
Effective temperature (T_{eff})	$6846 \pm 50 \text{ K}$
X	$0.741 \pm 0.004 \text{ dex}$
Z	$0.006 \pm 0.002 \text{ dex}$
Period (P) ^a	$0.545740 \pm 0.000007 \text{ days}$

^aThe period is determined using the Kepler light-curve with PERIOD-04 (Lenz & Breger 2005).

6 APPLICATIONS OF ANN INTERPOLATORS

6.1 Light Curve Comparison of EZ Cnc

As an application to the ANN interpolator, we generated and compared the light curve of an RRab star ‘EZ Cnc’ or ‘EPIC 212182292’ with the observed light curve. It is a non-Blazko RRab variable star which has been observed extensively in both photometric and spectroscopic observing regimes. Wang et al. (2021) used 55 high-quality Large Sky Area Multi-Object Fiber Spectroscopic Telescope (LAMOST, Luo et al. 2015) spectra of medium resolution to determine the atmospheric parameters (T_{eff} , $\log g$, and $[M/H]$). Starting from these parameters, they generated a grid of theoretical models using MESA, applying the time-dependent turbulent convective models. They searched for the optimum parameters for which the modelled light curve matched with the observed light curve from the K2 mission (Howell et al. 2014) of the *Kepler* spacecraft for which the light curve was processed by EPIC Variability Extraction and Removal for Exoplanet Science Targets Pipeline (EVEREST; Luger et al. 2016). The estimated parameters of the star are given in Table 7. The given flux was converted to the *Kepler* magnitude (Kp) by formula given by Nemec et al. (2011),

$$Kp = m_0 - 2.5 \log(\text{Flux})$$

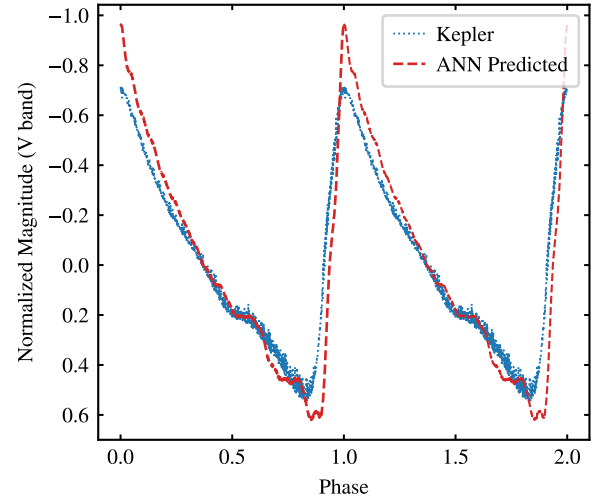
where $m_0 = 25.4$ is derived by taking the difference between the instrument magnitude and the mean of Kp (Wang et al. 2021). We converted the Kp to the V band magnitude using the relation given by Nemec et al. (2011),

$$V = (1.45 \pm 0.24)Kp - (5.97 \pm 3.20)$$

After extracting the V band light curve, we did extinction correction using the reddening maps of Schlegel et al. (1998); Schlafly & Finkbeiner (2011) and found $E(B-V) = 0.027 \pm 0.0006$ and the corresponding $A_V = 3.32 \times 0.0272 \pm 0.0006 = 0.0903 \pm 0.0020$ ³ using equation 10.

We generated a light curve using the V band interpolator by providing the parameters given in Table 7 as input. The error bars for the predicted magnitude are derived from the given uncertainties in the physical parameters. The resulting ANN generated light curve is plotted against the observed V band light curve from the *Kepler* telescope in Fig. 11. For the purpose of comparison, both light curves are normalised to mean magnitudes. We also did the quantitative analysis by determining and comparing the Fourier amplitude and phase parameter ratio for the *Kepler* V band, and ANN predicted V band light curve. The derived parameters including amplitudes and Fourier parameter ratios are given in Table 8. The peak-to-peak

³ The values are determined from NASA/IPAC INFRARED SCIENCE ARCHIVE (<https://irsa.ipac.caltech.edu/applications/DUST/>).

**Figure 11.** This plot represents the observed light curve from the K2 survey (converted to V band) along with the ANN generated light curve using the trained V band interpolator.**Table 8.** Comparison of the Fourier parameters of EZ Cnc star derived using K2 and ANN predicted light curve.

	K2 light curve (Kp band converted to V band)	ANN Predicted (V band)
A (mag)	1.263 ± 0.148	1.584 ± 0.107
mean mag (mag)	11.988 ± 0.002	0.703 ± 0.002
R_{21}	0.516 ± 0.002	0.542 ± 0.005
R_{31}	0.327 ± 0.002	0.325 ± 0.005
R_{41}	0.153 ± 0.002	0.223 ± 0.005
R_{51}	0.104 ± 0.002	0.178 ± 0.005
ϕ_{21}	2.761 ± 0.005	2.783 ± 0.013
ϕ_{31}	5.719 ± 0.007	5.718 ± 0.020
ϕ_{41}	2.214 ± 0.013	2.170 ± 0.027
ϕ_{51}	5.024 ± 0.018	5.119 ± 0.034

amplitude (A) predicted by the ANN V band interpolator is higher than the observed V band light curve. This is due to a rather low mixing length parameter adopted in the considered grid of models. For a successful model fitting applications to RR Lyrae stars (see e.g. Marconi & Clementini 2005; Marconi & Degl’Innocenti 2007), an increased mixing length value is required to match the light curves of fundamental pulsators. The Fourier amplitude and phase ratio of the K2 and ANN generated light curves match each other within the 1σ errors.

A direct application of this analysis is to estimate the distance to the star. Since we have calculated the mean absolute magnitude from the ANN generated light curve and the apparent magnitude from the *Kepler* telescope, the distance modulus is calculated as $\mu_{\text{EZ Cnc}} = 11.988(2) - 0.703(2) = 11.284(3) \text{ mag}$, and hence the distance d (in pc) calculated using the $\mu = 5 \log(d) - 5$ gives $d = 1806 \pm 2 \text{ pc}$. The calibrated *Gaia* DR2 distance for this star is $1840_{-161}^{+192} \text{ pc}$ (Bailer-Jones et al. 2018), which is recently updated by *Gaia* EDR3 to $1775_{-70}^{+70} \text{ pc}$ (Bailer-Jones et al. 2021). The estimated distance to the EZ Cnc remarkably matches with the published distance estimations in the literature.

Table 9. The parameter space of the new grid generated using the trained ANN Interpolators.

Parameter	Range	Step
M	0.52 - 0.79 M_{\odot}	0.03 M_{\odot}
$\log(L/L_{\odot})$	1.54 - 2.02 dex	0.04 dex
T_{eff}	5300 - 7000 K	100 K
Y	[0.245, 0.25, 0.265]	
Z	[0.00011, 0.00668, 0.01324, 0.01980]	

6.2 Generating a grid of models using the trained ANN interpolators

To get the precise physical parameters of pulsating variable stars, a grid of model light curves is compared with the observed light curve. However, a pre-computed grid of models is usually very coarse and non-uniform in the parameter space. This is due to the high computation cost and time consuming process of solving time-dependent hydrodynamical equations of the stellar atmosphere. Moreover, to constrain the parameters like mass, surface gravity and metallicity, we need to rely on spectroscopic data which is usually not available with photometric data. Hence, a fine grid of models is required to pin down the physical and atmospheric parameters of the star.

We generated a fine grid of light curve templates in both I and V bands using the trained interpolators. The choice of input parameters for the new grid is limited by the parameter space of the original grid of models. We choose a finer and more uniform grid than the original models. We generated the grid for three helium abundance ratios $Y=0.245, 0.25,$ and 0.265 and 4 different Z values ranging from metal-poor to metal-rich stars. For any combination of Y and Z , the hydrogen abundance ratio (X) can be calculated using $X = 1 - Y - Z$. Mass (M) varies from 0.52 to $0.79 M_{\odot}$, with a constant step size of $0.03 M_{\odot}$. The luminosity parameter $\log(L/L_{\odot})$ varies from 1.54 to 2.02 dex, with a step size of 0.04 dex, the effective temperature (T_{eff}) ranges from 5300 to 7000 K with a step size of 100 K. The period of an RR Lyrae star is closely related to its temperature, luminosity, and mass van Albada & Baker (1971). The van Albada-Baker (vAB) relation describes this relationship. We have used a modern version of the vAB relation, which includes the effect of metallicity on the pulsation period, from Marconi et al. (2015). We used the relation for the fundamental mode RRLs.

$$\begin{aligned} \log P = & - (0.58 \pm 0.02) \log \left(\frac{M}{M_{\odot}} \right) + (0.860 \pm 0.003) \log \left(\frac{L}{L_{\odot}} \right) \\ & - (3.40 \pm 0.03) \log(T_{\text{eff}}) + (0.013 \pm 0.002) \log(Z) \\ & + (11.347 \pm 0.006). \end{aligned} \quad (13)$$

We end up with a grid of 37,800 individual parameter combinations for which the template light curves are generated in the I and V band using the interpolators. Fig. 12 represents the distribution of Marconi et al. (2015) parameter space with the new grid parameters that we have computed (see Table 9 for the parameter ranges). A complete distribution of all parameters is shown in Fig. A1. The light curve templates of six random models of the new grid are shown in Fig. 13 in both I and V bands. We observe that the predicted light curves exhibit the same structure and features as an RRab light curve. However, for certain combinations of the input parameters, the predicted light curve may not resemble an RRab light curve. The reason for this can be traced back to the scarcity of models in this region of the training dataset or the lack of stable RRab stars with these combinations of physical parameters.

7 SUMMARY

We present a new technique to generate the light curve of RRab models in different photometric bands using ANN. We built and trained an artificial neural network for interpolating the light curve within a pre-computed grid of models. The ANN has been trained with the physical parameters-light curve grid. We used the models generated by Marconi et al. (2015) and used in Das et al. (2018), which were computed by solving the hydrodynamical conservation equations simultaneously with a nonlocal, time-dependent treatment of convective transport (Stellingwerf 1982; Bono & Stellingwerf 1994; Bono et al. 2000a; Marconi 2009). For the validation of the trained interpolators, light curves for a few new models were generated and then compared with the ANN predicted light curves.

The architecture of the neural network is tuned using the I band light curves. A random search for the hyperparameters is performed within a grid of *inferred* hyperparameter combinations. The architecture and trained weights of the best-performing network are then adopted for making the final interpolators in I and V bands.

As an application of the trained interpolators, we generated and compared the light curves of the RRab stars in the Magellanic clouds (LMC/SMC). The physical parameters [$M/M_{\odot}, \log(L/L_{\odot}), T_{\text{eff}}$] of RRab stars in LMC and SMC are adopted from Bellinger et al. (2020). Z is calculated from the metallicity estimates provided by Skowron et al. (2016), and $X = 1 - Y - Z$; is calculated using a fixed primordial helium abundance ($Y = 0.245$). Lastly, the period is determined from the observed light curve using the ‘Lomb-scargle’ method. The interpolators are then used to predict the light curve from the given physical parameters. Both observed and predicted light curves are then fitted with a Fourier sine series (see eq. 6) with $N=5$. The comparison of ANN predicted amplitudes, Fourier amplitude ratios and Fourier phase differences with the observations is shown in Fig. 7, 8, & 9. We observe that ANN predicted amplitudes are a bit larger than the observed amplitudes and the reason for this can be traced back to the low mixing length that was used to compute the original models. The Fourier amplitude ratios (R_{k1} , as defined in eq. 8) of the light curves predicted by the ANN are in great agreement with observations, except for a few exceptions where R_{41} and R_{51} exhibit an additional feature in the ANN predicted models at around $\log(P) \approx -0.22$. The Fourier phase differences (ϕ_{k1} , defined in equation 9) are consistently shifted, particularly ϕ_{21} and ϕ_{31} . The cause of this discrepancy is not understood and it should be noted that even the state-of-the-art hydrodynamical code, MESA-rsp, is unable to accurately reproduce the Fourier phase differences (Paxton et al. 2019). We also determine the distances to the LMC and SMC based on the reddening independent Wesenheit index. The distances found ($\mu_{\text{LMC}} = 18.567 \pm 0.135$ mag, and $\mu_{\text{SMC}} = 18.93 \pm 0.17$ mag) are in excellent agreement with the published distances based on eclipsing binaries ($\mu_{\text{LMC}} = 18.476 \pm 0.024$ mag, and $\mu_{\text{SMC}} = 18.95 \pm 0.07$ mag; Graczyk et al. 2014; Pietrzyński et al. 2019).

To showcase the utility of the interpolators, we generated and compared the light curve of the RRab star EZ Cnc. The physical parameters of this star were determined by Wang et al. (2021) using medium-resolution spectroscopic observations from LAMOST and time-series photometric data from the *Kepler* mission. We transformed the *Kepler* light curve into the V -band light curve and then compared it with the light curve predicted by the ANN both qualitatively and quantitatively. The reported distance to this star, $\mu_{\text{EZ Cnc}} = 11.284(3)$, or $d = 1806 \pm 2$ pc, is in excellent agreement with the recently updated parallax measurement from *Gaia* EDR3 of 1775_{-70}^{+70} pc (Bailer-Jones et al. 2021).

The generation of a grid of model light curves using traditional

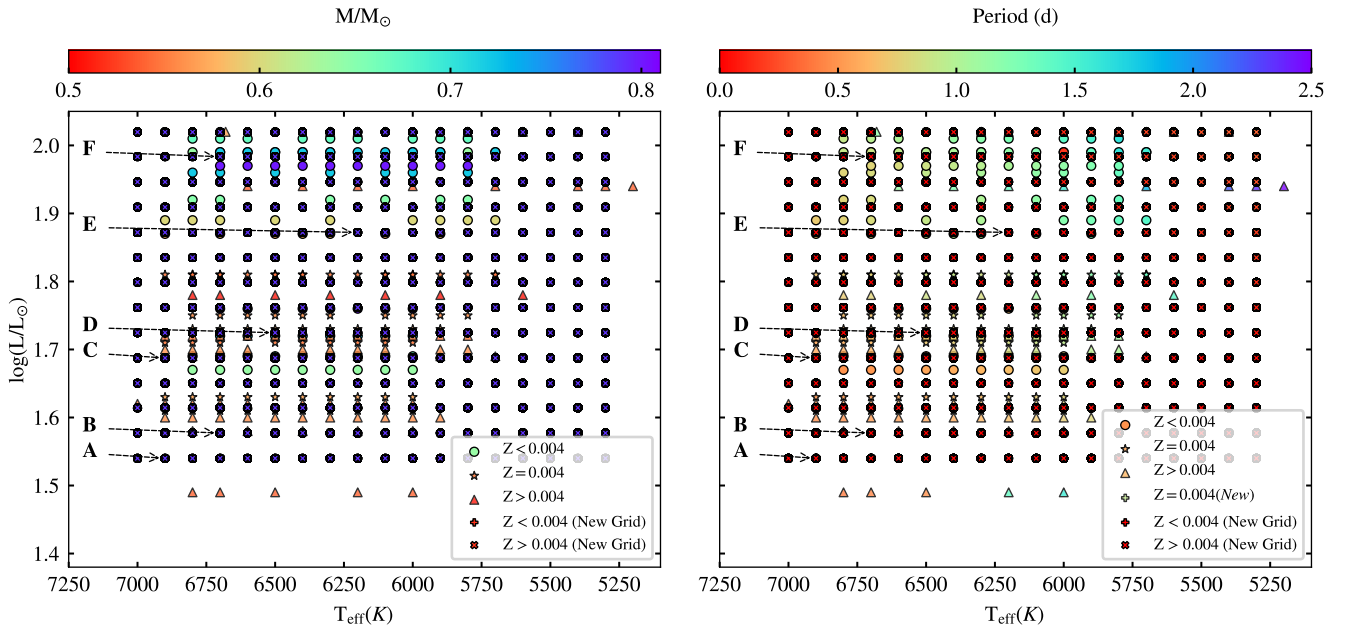


Figure 12. The parameter space of the new grid along with [Marconi et al. \(2015\)](#)'s original grid. A more detailed grid can be found in [Fig. A1](#). The ANN generated light curves of the labelled models are shown in [Fig. 13](#).

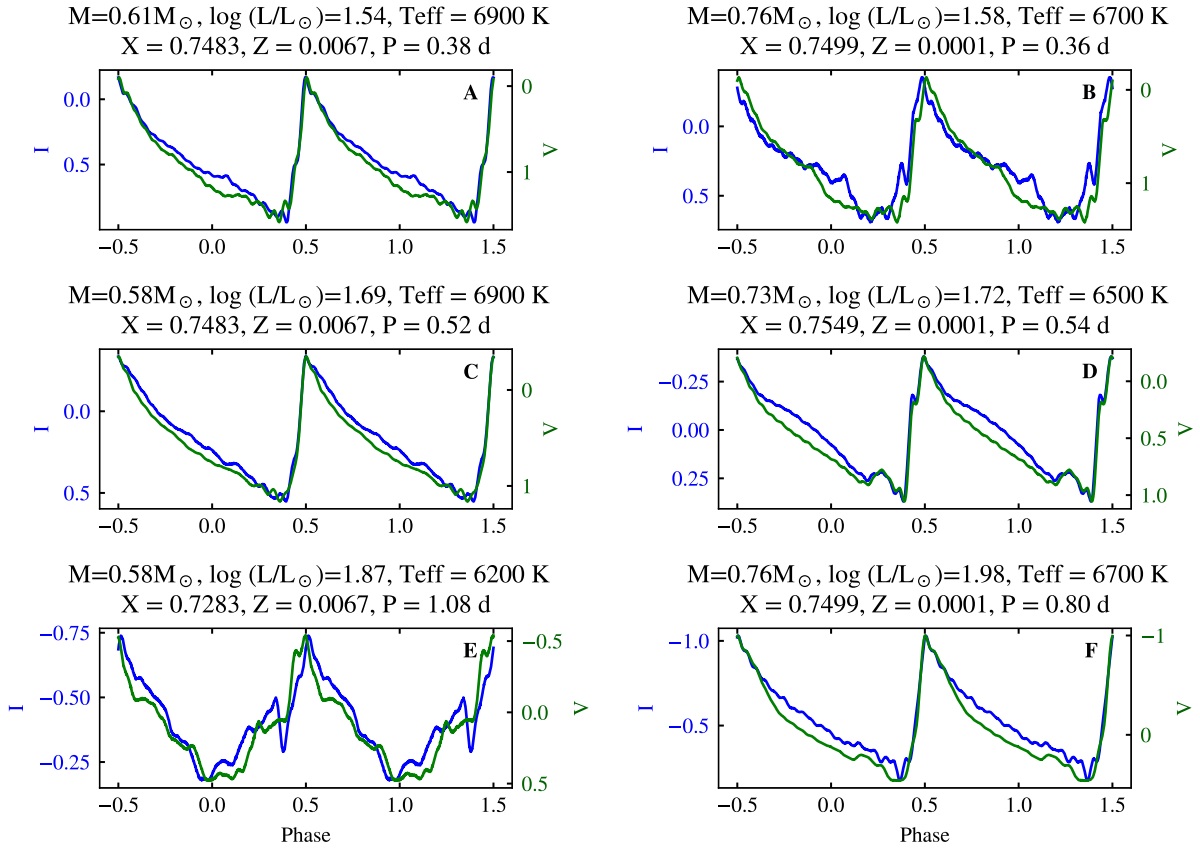


Figure 13. The ANN generated *I* and *V* band light curves for six models labelled in [Fig. 12](#).

methods can be computationally expensive and time-consuming, but by using the trained ANN interpolators, it is possible to generate a more dense grid of model light curves much more efficiently. The trained interpolators can generate a light curve given the input parameters, and the process is fast, taking only a few milliseconds for each light curve. Additionally, the size of the trained interpolator file is much smaller, making it easy to store and access. To complement existing theoretical model grids in the literature, a smooth grid of model light curves was generated using the trained interpolator. The grid of templates can be used in techniques such as template fitting to estimate the parameters of observed light curves. We generated over 30,000 model light curves in both the I and V bands, resulting in approximately 2 GB of data. However, if one has access to the trained interpolator file, which is much smaller in size (around 3.7 MB for each interpolator file in our case), it is also possible to generate a light curve by inputting the parameters. Generating each light curve takes only a few milliseconds (approximately 55 ms) for both I and V bands.

It is worth noting that our approach is dependent on the models used, and any errors or uncertainties in the models will be reflected in our results. However, this analysis will provide valuable insights into the stellar population model and has the potential to improve our understanding of these stars. The results can be improved by expanding the number of models or by using a more comprehensive grid of models. Additionally, the trained ANN models can be retrained on new or additional models to enhance the accuracy of the predicted light curves. In this way, our approach can be continuously refined and improved as more data and models become available.

SOFTWARE

We utilized various Python libraries in our study including Numpy (Harris et al. 2020), Pandas (McKinney 2010; team 2020), Astropy⁴ (Astropy Collaboration et al. 2013, 2018), TensorFlow (Martín Abadi et al. 2015), Matplotlib (Hunter 2007) and Seaborn (Waskom 2021). Numpy and Pandas were used for data manipulation, while Astropy, a community-developed package for Astronomy, was also utilized. TensorFlow was employed to implement the Artificial Neural Network, while Matplotlib and Seaborn were used for creating visual plots.

ACKNOWLEDGEMENTS

NK acknowledges the financial assistance from the Council of Scientific and Industrial Research (CSIR), New Delhi, as the Senior Research Fellowship (SRF) file no. 09/45(1651)/2019-EMR-I. AB acknowledges funding from the European Union's Horizon 2020 research and innovation programme under the Marie Skłodowska-Curie grant agreement No. 886298. SD acknowledges the KKP-137523 'SeismoLab' Élvonal grant of the Hungarian Research, Development and Innovation Office (NKFIH). HPS acknowledges a grant from the Council of Scientific and Industrial Research (CSIR) India, file no. 03(1428)/18-EMR-II.

DATA AVAILABILITY

Interested readers can use the trained interpolator to generate the predicted light curves of RRab stars using their input physical parameters. The generated grid of light curves is available on request and also through a web interface on <https://ann-interpolator.web.app/>.

REFERENCES

- Alexander D. R., Ferguson J. W., 1994, *ApJ*, 437, 879
- Asplund M., Grevesse N., Sauval A. J., 2005, in Barnes Thomas G. I., Bash F. N., eds, *Astronomical Society of the Pacific Conference Series Vol. 336, Cosmic Abundances as Records of Stellar Evolution and Nucleosynthesis*. p. 25
- Astropy Collaboration et al., 2013, *A&A*, 558, A33
- Astropy Collaboration et al., 2018, *AJ*, 156, 123
- Bailer-Jones C. A. L., Rybizki J., Fousneau M., Mantelet G., Andrae R., 2018, *AJ*, 156, 58
- Bailer-Jones C. A. L., Rybizki J., Fousneau M., Demleitner M., Andrae R., 2021, *AJ*, 161, 147
- Bellinger E. P., Kanbur S. M., Bhardwaj A., Marconi M., 2020, *MNRAS*, 491, 4752
- Bergstra J., Bengio Y., 2012, *Journal of machine learning research*, 13
- Bhardwaj A., 2022, *Universe*, 8, 122
- Bhardwaj A., Kanbur S. M., Singh H. P., Macri L. M., Ngeow C.-C., 2015, *MNRAS*, 447, 3342
- Bhardwaj A., Macri L. M., Rejkuba M., Kanbur S. M., Ngeow C.-C., Singh H. P., 2017a, *AJ*, 153, 154
- Bhardwaj A., Kanbur S. M., Marconi M., Rejkuba M., Singh H. P., Ngeow C.-C., 2017b, *MNRAS*, 466, 2805
- Bhardwaj A., et al., 2021, *ApJ*, 909, 200
- Bono G., Stellingwerf R. F., 1994, *ApJS*, 93, 233
- Bono G., Caputo F., Castellani V., Marconi M., 1997, *A&AS*, 121, 327
- Bono G., Caputo F., Marconi M., 1998, *ApJ*, 497, L43
- Bono G., Marconi M., Stellingwerf R. F., 1999, *ApJS*, 122, 167
- Bono G., Castellani V., Marconi M., 2000a, *ApJ*, 529, 293
- Bono G., Castellani V., Marconi M., 2000b, *ApJ*, 532, L129
- Bono G., Caputo F., Castellani V., Marconi M., Storm J., 2001, *MNRAS*, 326, 1183
- Caputo F., Castellani V., Degl'Innocenti S., Fiorentino G., Marconi M., 2004, *A&A*, 424, 927
- Catelan M., Pritzl B. J., Smith H. A., 2004, *ApJS*, 154, 633
- Clementini G., Gratton R., Bragaglia A., Carretta E., Fabrizio L. D., Maio M., 2003, *The Astronomical Journal*, 125, 1309
- Coppola G., et al., 2011, *MNRAS*, 416, 1056
- Cusano F., et al., 2013, *ApJ*, 779, 7
- Cybenko G., 1989, *Mathematics of Control, Signals and Systems*, 2, 303
- Das S., Bhardwaj A., Kanbur S. M., Singh H. P., Marconi M., 2018, *Monthly Notices of the Royal Astronomical Society*, 481, 2000
- Das S., et al., 2020, *Monthly Notices of the Royal Astronomical Society*, 493, 29
- De Somma G., Marconi M., Molinaro R., Cignoni M., Musella I., Ripepi V., 2020, *ApJS*, 247, 30
- De Somma G., Marconi M., Molinaro R., Ripepi V., Leccia S., Musella I., 2022, *ApJS*, 262, 25
- Deb S., Singh H. P., 2009, *A&A*, 507, 1729
- Di Criscienzo M., et al., 2011, *AJ*, 141, 81
- Drake A. J., et al., 2013, *ApJ*, 763, 32
- Draper N. R., Smith H., 1998, *Applied regression analysis*. Vol. 326, John Wiley & Sons
- Elsken T., Metzner J. H., Hutter F., 2019, *The Journal of Machine Learning Research*, 20, 1997
- Feuchtinger M. U., 1999, *A&AS*, 136, 217
- Fiorentino G., et al., 2010, *ApJ*, 708, 817
- Glantz S. A., Slinker B. K., 2001, *Primer of applied regression & analysis of variance*, ed. McGraw-Hill, Inc., New York

⁴ <http://www.astropy.org>

- Graczyk D., et al., 2014, *ApJ*, 780, 59
- Guo X., Yang J., Wu C., Wang C., Liang Y., 2008, *Neurocomputing*, 71, 3211
- Harris C. R., et al., 2020, *Nature*, 585, 357
- Haschke R., Grebel E. K., Duffau S., 2011, *AJ*, 141, 158
- Hornik K., 1991, *Neural Networks*, 4, 251
- Hornik K., Stinchcombe M., White H., 1989, *Neural Networks*, 2, 359
- Howell S. B., et al., 2014, *PASP*, 126, 398
- Hunter J. D., 2007, *Computing in Science & Engineering*, 9, 90
- Iglesias C. A., Rogers F. J., 1996, *ApJ*, 464, 943
- Jurcsik J., Kovacs G., 1996, *A&A*, 312, 111
- Jurcsik J., et al., 2015, *The Astrophysical Journal Supplement Series*, 219, 25
- Keller S. C., Wood P. R., 2002, *ApJ*, 578, 144
- Kingma D. P., Ba J., 2014, arXiv e-prints, p. arXiv:1412.6980
- Kuehn C. A., et al., 2013, arXiv e-prints, p. arXiv:1310.0553
- Kunder A., et al., 2013, *AJ*, 146, 119
- Lenz P., Breger M., 2005, *Communications in Asteroseismology*, 146, 53
- Lomb N. R., 1976, *Ap&SS*, 39, 447
- Longmore A. J., Fernley J. A., Jameson R. F., 1986, *MNRAS*, 220, 279
- Luger R., Agol E., Kruse E., Barnes R., Becker A., Foreman-Mackey D., Deming D., 2016, *AJ*, 152, 100
- Luo A.-L., et al., 2015, *Research in Astronomy and Astrophysics*, 15, 1095
- Madore B. F., 1982, *ApJ*, 253, 575
- Marconi M., 2009, in Guzik J. A., Bradley P. A., eds, *American Institute of Physics Conference Series Vol. 1170, Stellar Pulsation: Challenges for Theory and Observation*. pp 223–234 (arXiv:0909.0900), doi:10.1063/1.3246450
- Marconi M., Clementini G., 2005, *AJ*, 129, 2257
- Marconi M., Degl’Innocenti S., 2007, *A&A*, 474, 557
- Marconi M., Caputo F., Di Criscienzo M., Castellani M., 2003, *ApJ*, 596, 299
- Marconi M., Bono G., Caputo F., Piersimoni A. M., Pietrinferni A., Stellingwerf R. F., 2011, *ApJ*, 738, 111
- Marconi M., Molinaro R., Ripepi V., Musella I., Brocato E., 2013, *MNRAS*, 428, 2185
- Marconi M., et al., 2015, *The Astrophysical Journal*, 808, 50
- Marconi M., et al., 2017, *MNRAS*, 466, 3206
- Marconi M., Bono G., Pietrinferni A., Braga V. F., Castellani M., Stellingwerf R. F., 2018, *ApJ*, 864, L13
- Martín Abadi et al., 2015, *TensorFlow: Large-Scale Machine Learning on Heterogeneous Systems*
- McKinney W., 2010, in Walt S. v. d., Millman J., eds, *Proceedings of the 9th Python in Science Conference*. pp 56 – 61, doi:10.25080/Majora-92bf1922-00a
- Moretti M. I., et al., 2009, *ApJ*, 699, L125
- Mullen J. P., et al., 2021, *ApJ*, 912, 144
- Muraveva T., et al., 2015, *ApJ*, 807, 127
- Natale G., Marconi M., Bono G., 2008, *ApJ*, 674, L93
- Nemec J. M., et al., 2011, *MNRAS*, 417, 1022
- Nemec J. M., Cohen J. G., Ripepi V., Derekas A., Moskalik P., Sesar B., Chadid M., Bruntt H., 2013, *ApJ*, 773, 181
- O’Malley T., Bursztein E., Long J., Chollet F., Jin H., Invernizzi L., others 2019, *KerasTuner*, <https://github.com/keras-team/keras-tuner>
- Paxton B., Bildsten L., Dotter A., Herwig F., Lesaffre P., Timmes F., 2011, *ApJS*, 192, 3
- Paxton B., et al., 2013, *ApJS*, 208, 4
- Paxton B., et al., 2015, *ApJS*, 220, 15
- Paxton B., et al., 2018, *ApJS*, 234, 34
- Paxton B., et al., 2019, *ApJS*, 243, 10
- Piersanti, L. Straniero, O. Cristallo, S. 2007, *A&A*, 462, 1051
- Pietrinferni A., Cassisi S., Salaris M., Castellani F., 2006, *ApJ*, 642, 797
- Pietrukowicz P., et al., 2015, *ApJ*, 811, 113
- Pietrzyński G., et al., 2019, *Nature*, 567, 200
- Ragosta F., et al., 2019, *MNRAS*, 490, 4975
- Ruder S., 2016, *An overview of gradient descent optimization algorithms*
- Rumelhart D. E., Hinton G. E., Williams R. J., 1986, *nat*, 323, 533
- Sandage A., Katem B., Sandage M., 1981, *The Astrophysical Journal Supplement Series*, 46, 41
- Scargle J. D., 1982, *ApJ*, 263, 835
- Schlafly E. F., Finkbeiner D. P., 2011, *ApJ*, 737, 103
- Schlegel D. J., Finkbeiner D. P., Davis M., 1998, *ApJ*, 500, 525
- Serenelli A. M., Basu S., 2010, *The Astrophysical Journal*, 719, 865
- Skowron D. M., et al., 2016, *Acta Astron.*, 66, 269
- Smolec R., Moskalik P., 2008, *Acta Astron.*, 58, 193
- Sollima A., Borissova J., Catelan M., Smith H. A., Minniti D., Cacciari C., Ferraro F. R., 2006, *ApJ*, 640, L43
- Soszyński I., et al., 2009, *Acta Astron.*, 59, 1
- Soszyński I., et al., 2016, *Acta Astron.*, 66, 131
- Soszyński I., et al., 2017, arXiv preprint arXiv:1712.01307
- Soszyński I., et al., 2018, *Acta Astron.*, 68, 89
- Steel R. G. D., Torrie J. H., others 1960, *Principles and procedures of statistics*.
- Stellingwerf R. F., 1982, *ApJ*, 262, 339
- Stellingwerf R. F., 1984, *ApJ*, 284, 712
- Vivas A. K., Zinn R., 2006, *AJ*, 132, 714
- Wang J., Fu J.-N., Zong W., Wang J., Zhang B., 2021, *MNRAS*, 506, 6117
- Waskom M. L., 2021, *Journal of Open Source Software*, 6, 3021
- Zinn R., Horowitz B., Vivas A. K., Baltay C., Ellman N., Hadjiyska E., Rabinowitz D., Miller L., 2014, *ApJ*, 781, 22
- team T. p. d., 2020, *pandas-dev/pandas: Pandas*, doi:10.5281/zenodo.3509134, <https://doi.org/10.5281/zenodo.3509134>
- van Albada T. S., Baker N., 1971, *ApJ*, 169, 311

APPENDIX A: INPUT DISTRIBUTION

A detailed input distribution of the input parameters is shown in Fig. A1. We have also shown the detailed distribution of parameters of the new grid for which the template light curves are generated.

This paper has been typeset from a $\text{\TeX}/\text{\LaTeX}$ file prepared by the author.

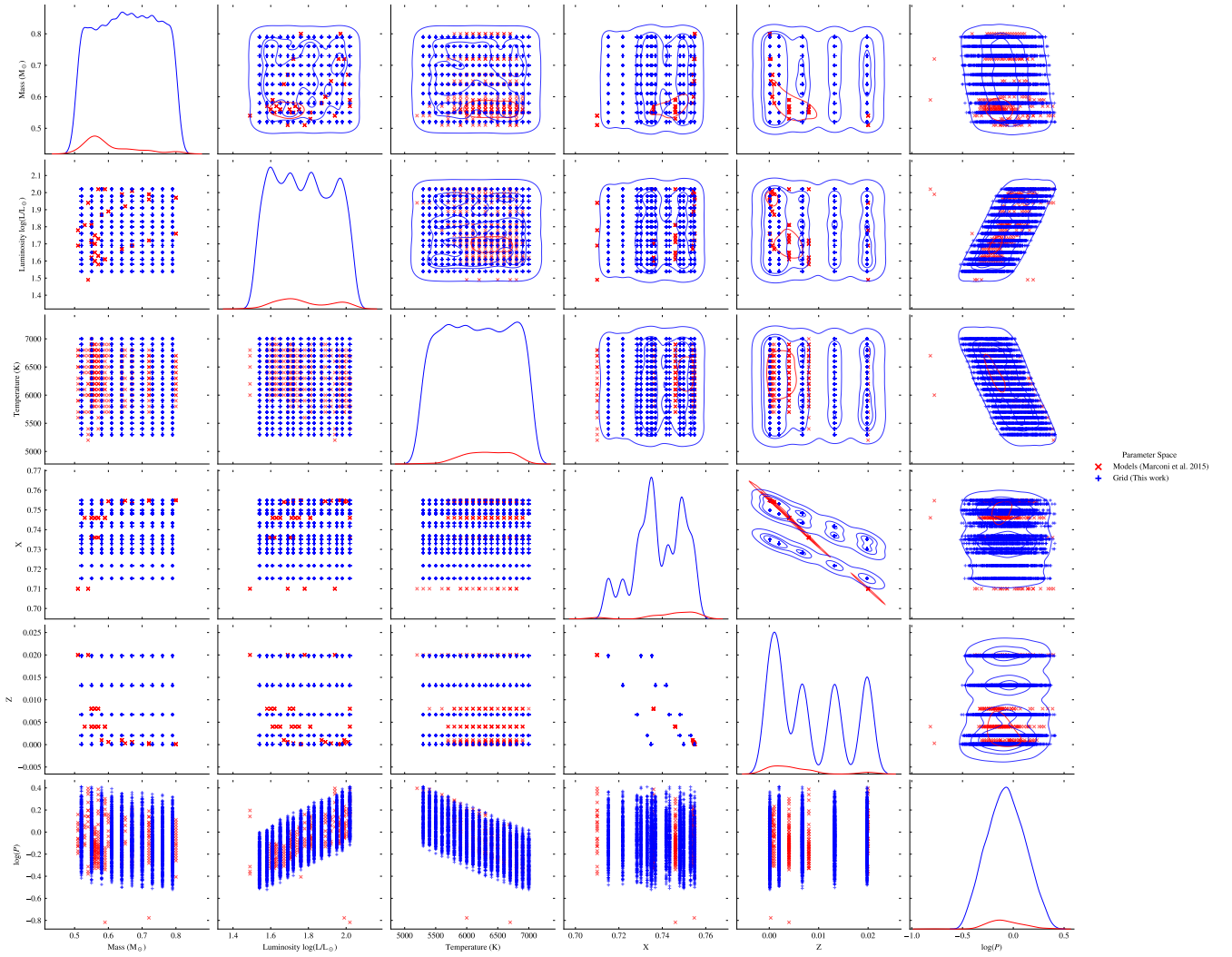


Figure A1. A pair plot with KDE (Kernel Density Estimation) plots in the upper triangle shows the relationship between six variables, namely mass, luminosity, effective temperature, X, Z, and $\log(P)$. The contours represent the parameter space in 2D for the given combination of six parameters. The plot is divided into subplots, with each subplot representing a pair-wise scatter plot of the six variables. The diagonal of the subplots shows the distribution of each variable using KDE plots. The red cross ('x') marker is assigned for the original models of Marconi et al. (2015) and the blue plus ('+') marker is assigned for the models generated in this work.